Cell type-specific inhibitory modulation of sound processing in the auditory thalamus.

Rolón-Martínez, S[1]., Mendoza, A.J.[2], Angeloni, C.F.[1], Vogler, N.W. [1], Chen, R.[1], Vu, K. [2], Haas, J.S.[2#], Geffen M.N.[1#] *

[1]*Department of Otorhinolaryngology, University of Pennsylvania, Philadelphia, PA, United States*

[2]*Department of Biological Sciences, Lehigh University, Bethlehem, PA, United States*

 # These authors contributed equally.

*Corresponding author:
Maria Neimark Geffen, Ph.D. (she/her)
Department of Otorhinolaryngology
Perelman School of Medicine
University of Pennsylvania
5 Ravdin
3400 Spruce St.
Philadelphia PA 19104
Tel.: 215.898.0782

ABSTRACT

Inhibition plays an important role in controlling the flow and processing of auditory information throughout the central auditory pathway, yet how inhibition shapes auditory processing in the medial geniculate body (MGB), the key region in the auditory thalamus, is poorly understood. MGB gates the flow of auditory information to the auditory cortex, and it is inhibited largely by the thalamic reticular nucleus (TRN). The TRN comprises two major classes of inhibitory neurons: parvalbumin (PV^{TRN})-positive and somatostatin (SST^{TRN})-positive neurons. PV and SST neurons have been shown to play differential roles in controlling sound responses in other brain regions. In the somatosensory and visual subregions of the TRN, PV^{TRN} and SST^{TRN} neurons exhibit anatomical and functional differences. However, it remains unknown whether and how PV^{TRN} and SST^{TRN} neurons differ in their anatomical projections from the TRN, and whether and how they differentially modulate activity in the MGB. We find that PV^{TRN} and SST^{TRN} neurons exhibit differential projection patterns within the thalamus: PV^{TRN} neurons predominantly project to ventral MGB, whereas SST^{TRN} neurons project to the dorso-medial regions of MGB. Furthermore, PV^{TRN} and SST^{TRN} neurons bi-directionally modulate sound responses in MGB. Selective optogenetic inactivation of PV^{TRN} neurons increased sound-evoked activity in over a third of MGB neurons, while another large fraction of neurons showed suppressed activity. In contrast, inactivating SST^{TRN} neurons largely reduced tone-evoked activity in MGB neurons. Cell type-specific computational models identified candidate circuit mechanisms for generating the bi-directional effects of TRN inactivation on MGB sound responses. These distinct inhibitory pathways within the auditory thalamus reveal a cell type-specific role for thalamic inhibition in auditory computation.

40 # INTRODUCTION

41 Inhibition is crucial to sensory information processing and transmission in the brain. In the auditory
42 system, inhibition plays a critical role in shaping auditory computations, from sound localization in the
43 brainstem to statistical inference in the auditory cortex[1–7]. There are many different inhibitory neuron types
44 within the central auditory pathway which differ morphologically, electrophysiologically, and functionally.
45 In auditory cortex, two major sub-classes of inhibitory neurons, parvalbumin- (PV) and somatostatin- (SST)
46 positive neurons, play distinct functional roles[8–16], and activating PV or SST neurons leads to a decrease in
47 frequency selectivity and an overall increase in tone responsiveness of cortical excitatory neurons[10,13,17,18].
48 SST, but not PV, neurons contribute to stimulus-specific adaptation, a phenomenon in which neurons adapt
49 selectively to a subset of inputs presented frequently[8,9,19–23].

50 However, cortical neurons are not the only cells that receive targeted inhibition along the auditory
51 pathway. The medial geniculate body (MGB) located within the thalamus receives auditory information from
52 the auditory brainstem, and MGB neurons shape and relay sensory information to auditory cortex[24,25]. This
53 ascending projection from MGB to auditory cortex is shaped by inhibition from the thalamic reticular
54 nucleus (TRN), a thin sheet of inhibitory neurons that targets and envelops the thalamus[26–30]. Anatomically,
55 the TRN receives excitatory collaterals from the MGB as well as from corticothalamic L5 and L6 neurons,
56 and sends feedforward inhibition back to MGB[27,31–35]. Functionally, the TRN filters relevant sensory
57 information important for perception[36–38] and supports optimal behavioral performance in sensory
58 attentional tasks[39–41].

59 The TRN contains multiple types of inhibitory neurons, predominantly PV and SST positive neurons.
60 Recent findings in TRN subregions dedicated to visual and somatosensory modalities have described
61 segregated distributions of distinct inhibitory neuron subtypes that differentially target distinct thalamic
62 nuclei and exhibit differences in intrinsic and synaptic properties[42–45]. Thus, it is plausible that as a result
63 of both organizational and functional differences, PV^{TRN} and SST^{TRN} neurons might differentially exert
64 inhibitory control of sound processing in the MGB. However, the specific roles of PV^{TRN} and SST^{TRN} neurons
65 in gating the auditory thalamocortical relay have not been systematically tested.

66 In this study, we examined the differential effects of PV^{TRN} and SST^{TRN} neurons on thalamic sound
67 processing[46]. To anatomically identify how PV^{TRN} and SST^{TRN} neurons project to the sub-nuclei of the MGB,
68 we used viral tracing techniques to express an anterograde virus encoding a flexed fluorescent reporter in

69 TRN of transgenic PV-Cre or SST-Cre mouse lines and traced projections to the MGB. We found that PV^{TRN}
70 and SST^{TRN} neurons target distinct subregions of the MGB and differentially modulate neuronal activity. We
71 used viral transfection to drive a soma-targeted inhibitory opsin in the TRN to inactivate PV^{TRN} or SST^{TRN}
72 neurons while recording neuronal activity from neurons in the MGB of awake passively listening head-fixed
73 mice. Inactivating PV cells resulted in a mix of enhanced and suppressed MGB responses. By contrast,
74 inhibiting SST enhanced only a small percentage of MGB responses, but suppressed the vast majority of
75 responses. To identify candidate circuit mechanisms that could underlie the unexpected bidirectional
76 modulation resulting from inactivation of SST^{TRN} and PV^{TRN} neurons, we examined changes in MGB activity
77 in computational models with varied synaptic connectivity within TRN and from TRN to MGB. These
78 simulations revealed several variations of underappreciated thalamic circuitry that can explain the
79 experimental results, including disynaptic inhibition and underappreciated divergent inhibition. Together,
80 our results demonstrate cell and circuit specificity of inhibition within the auditory thalamus that is likely to
81 influence auditory perception.
82

83 ## MATERIALS AND METHODS

84 *Animals.*

85 We performed all experimental procedures in accordance with NIH guidelines on use and care of
86 laboratory animals and by approval of the Institutional Animal Care and Use Committee at the University
87 of Pennsylvania (protocol number 803266). Care was taken to minimize any pain, discomfort, or distress of
88 the animals during and following experiments. Experiments were performed in adult male (n = 12) and
89 female (n = 12) mice aged 3-8 months and weighing 20-32g. The mouse lines used in this study were crosses
90 between Cdh23 mice (B6.CAST-$Cdh23^{Ahl+}$/Kjn; RRID:IMSR_JAX:002756)—a transgenic line that has a
91 targeted point reversion in the Cdh23 gene which protects mice from age-related hearing loss[47]—and PV-
92 Cre mice (B6.129P2-$Pvalb^{tm1(cre)Arbr}$/J; RRID:IMSR_JAX:017320) or SST-Cre mice ($SST^{tm2.1(cre)Zjh}$/J;
93 RRID:IMSR_JAX:013044). Mice were housed at 28°C on a reversed 12hr light-dark cycle with ad libitum
94 access to food and water. Experiments were performed during the animals' dark cycle and housed
95 individually in an enriched environment after major surgery. Euthanasia was performed by infusion of a
96 ketamine (300mg/kg) and dexmedetomidine (3mg/kg) or prolonged exposure to CO2. Both methods are

97 consistent with the recommendations of the American Veterinary Medical Association (AVMA) Guidelines
98 on Euthanasia.
99
100 *Surgical Procedures.*
101 Mice were induced to a surgical plane of anesthesia with 3% isoflurane in oxygen and secured in a
102 stereotaxic frame. Animals were then maintained in an anesthetic plane with 1-2% isoflurane in oxygen and
103 kept at a body temperature of 36°C with the use of a homeothermic blanket. Prior to any surgical procedure,
104 mice were administered subcutaneous injections of sustained release buprenorphine (1mg/kg) for analgesia,
105 dexamethasone (0.2mg/kg) for reduction of swelling, and bupivacaine (2mg/kg), for local anesthesia. Mice
106 received a subcutaneous injection of an antibiotic, enrofloxacin (Baytril; 5mg/kg), for 3 days as part of their
107 post-operative care.
108
109 *Viral Injections.*
110 Approximately 21 days prior to electrophysiological recordings or transcardial perfusions, we
111 performed small (0.5mm in diameter) unilateral craniotomies using a micromotor drill (Foredom)–under
112 aseptic conditions–over auditory TRN (audTRN) or MGB. Glass syringes attached to a syringe pump (Pump
113 11 Elite, Harvard Apparatus) were backfilled with modified viral vectors, placed over the brain region of
114 interest, and used to inject virus at 60nL/min. Glass syringes were made using a micropipette puller (P-97,
115 Sutter Instruments) from glass capillaries (Harvard Apparatus, 30-0038) with tip openings ranging from
116 30µm-40µm in diameter. Following injections, syringes were left in place for 15-20min before retraction.
117 Craniotomies were then covered with bone wax (Fine Science Tools) or a removable silicone plug (Kwik-
118 Cast, World Precision Instruments). The coordinates used to target audTRN were: -1.80mm posterior to
119 bregma, ±2.25mm lateral to bregma, -2.90mm below the pial surface. The MGB coordinates used were: -
120 3.30mm posterior to bregma, ±2.00mm lateral to bregma, -2.90mm below the pial surface. Viral spread was
121 confirmed post-mortem.
122
123 *Viral Vectors.*
124 For soma-targeted inactivation of PV or SST neurons of the audTRN we injected 400nL of AAV5-hSyn1-
125 SIO-stGtACR1-FusionRed (≥7×10^{12} vg/mL, Addgene 105678-AAV5). For anterograde tracing of PV or SST

126 neurons of the audTRN and control experiments we injected 250nL or 400nL of AAV5-hSyn-DIO-mCherry
127 (≥ 7×10^{12} vg/mL, Addgene 50459-AAV5).
128
129 *Fiber Optic Cannula & Headpost Implantation.*
130 Following virus injections, fiber optic cannulas (Prizmatix: 3mm in length, 1.25mm in diameter,
131 Ø200µm core, 0.66NA) were implanted above audTRN at a 20° angle, -1.80mm posterior to bregma,
132 ±3.25mm lateral to bregma, and -2.50mm below the pial surface. A small craniotomy was made over the left
133 frontal lobe and a ground pin was implanted. Craniotomies were sealed with Kwik-Cast (World Precision
134 Instruments). The cannula, ground pin and a custom-made stainless-steel headpost (eMachine shop) were
135 then secured with dental cement (C&B Metabond, Parkell) and dental acrylic (Lang Dental).
136
137 *Tissue Processing.*
138 After allowing time for proper viral expression or following electrophysiological recordings, mice
139 were deeply anesthetized with a cocktail of ketamine and dexmedetomidine (see Animals) and transcardially
140 perfused with 1X PBS followed by 4% paraformaldehyde (PFA) in PBS. Brains were extracted and post-fixed
141 in 4% PFA overnight at 4°C. Following post-fixation, tissue was cryoprotected in 30% sucrose for at least
142 24hrs at 4°C until sectioning. Brain sections of 40µm-50µm in thickness were cut on a cryostat (Leica
143 CM1860) and collected for immunohistochemistry or imaging of viral expression. For imaging of viral
144 expression or probe location, 50µm-thick sections were mounted on gelatin-coated glass slides and
145 coverslipped using ProLong Diamond Antifade Mounting media with DAPI (Catalog # P36971, Invitrogen).
146 For immunohistochemistry, 40µm-thick sections were collected in 12-well plates filled with 1X PBS (~5-10
147 sections per well). Slides were imaged using a fluorescent microscope (Leica DM6 B) or a confocal
148 microscope (Zeiss LSM 800).
149
150 *Immunohistochemistry.*
151 Free-floating 40µm-thick brain sections were first washed in 1X PBS (3 x 10min washes). To increase
152 membrane permeability, sections were microwaved for approximately 10 seconds and then incubated in a
153 solution of 0.3% Triton X-100 in 1X PBS (hereinafter referred to as PBT) for 30 min at room temperature.
154 The sections were then incubated in a blocking solution consisting of 5% normal goat serum in PBT

155 (hereinafter referred to as PBTG) for 30min-1hr at room temperature. Following incubation with PBTG,
156 sections were incubated in primary antibody solution which consisted of the following antibodies diluted in
157 PBTG: (1) 1:500 mouse monoclonal anti-Parvalbumin (Swant, PV-235; RRID:AB_10000343), (2) 1:500
158 rabbit polyclonal anti-Somatostatin (Immunostar, 20067); RRID: AB_572264), and (3) 1:1000 rabbit
159 polyclonal anti-Calretinin (Swant, Calretinin-7697; RRID:AB_2721226). Incubation in primary solution was
160 done overnight-48hrs at 4°C on a shaker (Fisher Scientific); well plates were covered with parafilm and a
161 plastic lid. Following the incubation period with primary antibody solution, sections were washed in PBT (3
162 x 10min washes). Sections were then incubated in secondary antibodies conjugated to fluorescent markers
163 diluted in PBTG for 2hrs at room temperature; well plates were covered with aluminum foil to block light.
164 Secondary antibodies used were: (1) Alexa Fluor Plus 488 Goat anti-Mouse IgG (H+L) (for PV stain; catalog
165 # A32723, Invitrogen; RRID: AB_2633275), (2) Alexa Fluor Plus 488 Goat anti-Rat IgG (H+L) (for SST
166 stain; Catalog # A48262, Invitrogen; RRID: AB_2896330), and (2) Alexa Fluor Plus 488 Goat anti-Rabbit
167 IgG (H+L) (for Calretinin stain; Catalog # A32731, Invitrogen; RRID: AB_2633280). Sections were then
168 incubated for 10min in a 1:40,000 dilution of DAPI stock solution in PBT (5mg/mL, Invitrogen; D1306).
169 The sections were subsequently washed in 1X PBS (5 x 10min washes). Sections were then mounted on
170 gelatin-coated glass slides, coverslipped using ProLong Diamond Antifade Mounting media (Catalog #
171 P36970, Invitrogen) and left to curate in the dark, on a flat surface at room temperature for at least 24hrs
172 prior to imaging. Slides were imaged using a fluorescent microscope (Leica DM6 B) or a confocal microscope
173 (Zeiss LSM 800).
174
175 *Acoustic Stimuli.*
176 Stimuli were generated using custom MATLAB code and were sampled at 200kHz with a 32-bit
177 resolution. Acoustic stimuli were delivered through a speaker (Multicomp by Newark, MCPCT-G5100-4139)
178 positioned in the direction of the animals' ear contralateral to the recording site. To assess stimulus-locked
179 auditory responses, we used a set of click trains made up of 5 broadband noise bursts at a rate of 1Hz. The
180 noise bursts were 25ms long and presented at a rate of 10Hz for a total of 500ms. To assess frequency
181 response functions in neuronal population, we generated a set of 19 pure tones of logarithmically spaced
182 frequencies ranging between 3kHz and 80kHz at 70dB sound pressure level relative to 20μPa (SPL). Each
183 tone was 50ms long with a 1ms cosine squared ramp, repeated 40 times with an inter-stimulus-interval of

184 300ms and presented in a pseudo-random order. 20 of those 40 tone repetitions were accompanied by a
185 continuous light pulse with a 1ms cosine squared ramp starting at tone onset and ending at tone offset (50ms
186 long; for details on light stimuli see Optogenetic Inactivation).
187
188 *Optogenetic Inactivation and Calibration.*
189 To inactivate populations of neurons, we injected a soma-targeted inhibitory opsin in the audTRN of
190 PV- and SST-Cre mice (see Viral Injections and Viral Vectors). Light-only recordings were achieved by
191 delivering continuous (1ms cosine squared ramp) light pulses of different durations (10ms, 25ms, 50ms, and
192 100ms) through an implanted fiber-optic cannula via a fiber-coupled blue LED (460nm, Prizmatix,
193 Optogenetics-LED-Blue). Frequency tuning Light_{On} trials were achieved by delivering a continuous 50ms
194 pulse with a 1ms squared ramp.
195 To reduce variability in the effects of optogenetic manipulation across mice, we developed a
196 procedure to calibrate the LED source prior to each recording session. Once the probe was in its final depth
197 for recording, we presented alternating click trains (see Acoustic Stimuli) wherein each trial consisted of a
198 click train without LED stimulation followed by a click train paired with LED stimulation with 20 different
199 intensities (LED driving voltage ranged from 0 to 5V) while recording neural responses. This stimulus set
200 was presented 10 times for each intensity value. Neural responses were sorted offline using Kilosort2. To
201 calculate if each unit was significantly sound responsive and discard noise clusters, we computed a Wilcoxon
202 sign-rank test between the sound responses during the LED-off click trains and a baseline period of activity.
203 Excluded units from further analysis are those whose P-values exceeded a Bonferroni-corrected α-level of
204 $0.05/n_{\text{clusters}}$. We then calculated the number of spikes during the LED_{off} click train trials (n_{OFF}) and during
205 the LED_{on} click train trials (n_{ON}) and computed the percent change in the response (r_{PC}) for each light
206 intensity:

207 $$r_{\text{PC}} = \frac{n_{\text{ON}} - n_{\text{OFF}}}{n_{\text{OFF}}} * 100$$

208 Using a logistic function, we fit the response function as a function of the LED voltage,

209 $$y = a + \frac{b}{1 + e^{-(x-c)d}}$$

210 where a determines the y-offset of the response, b determines the range of the response, c determines the x-
211 offset, and d determines the gain of the response. With this fit equation, we found the voltage values that

212 elicited a 100% increase (2-fold change) in neural spiking and used that value for the rest of the stimulus
213 presented in each individual recording session (0.1-5mW). Some sessions did not show a 2-fold increase
214 with LED manipulation; for these sessions we used maximum LED power (5mW) for all stimuli.
215
216 *Acute Electrophysiological Recordings.*
217 All electrophysiological recordings were carried out in a double-walled acoustic-isolation booth
218 (Industrial Acoustics). At least 21 days post-viral injection, animals were anesthetized (see Surgical
219 Procedures) and a small craniotomy (1mm in diameter) was performed using a micromotor drill (Foredom)
220 over MGB (for coordinates see Viral Injections). Mice were then clamped into a custom base and allowed to
221 recover from anesthesia for at least 30min. Following their recovery time, we vertically (0° on stereotaxic
222 arm) lowered a 32-channel silicon probe (NeuroNexus: A1x32-Poly2-10mm-50s-177) to a depth of ~3.5mm
223 from the pial surface using a motorized micromanipulator (Scientifica) attached to a stereotaxic arm (Kopf)
224 at a rate of 1-2μm/s. While we lowered the probe, a train of brief broadband noise clicks were played (see
225 Acoustic Stimuli), if we observed stimulus-locked responses, we determined the probe was in a sound-
226 responsive area. The probe was coated in lipophilic far-red dye (Vybrant DiD, Invitrogen), to determine
227 recording sites post-hoc (see Tissue Processing; Figure 2C). Recordings that did not display stimulus-locked
228 responses or were not determined to be in MGB were not used in this analysis. Once the probe reached the
229 target recording depth, it was left to settle in the brain for at least 30min prior to recording. Neural signals
230 were amplified via an Intan headstage (RHD 32ch, Intan Technologies), recorded at a rate of 30kHz using
231 an OpenEphys acquisition board and GUI[48], and digitized with an SPI cable. Signals were filtered between
232 500 and 6000Hz, offset corrected, and re-referenced to the median of all active channels. Recorded neural
233 data were spike sorted using KiloSort2[49] and manually corrected using phy2. Upon manual correction, units
234 were classified as either single- or multi- units; if units exhibited a clear refractory period, they were labeled
235 single units, otherwise they were classified as multi-units. Both single-units and multi-units were included
236 in all analyses (for number of units used see Table 1). Approximately 3 recording sessions were achieved
237 from each individual mouse at different recording sites.
238
239 *Gray Value Analysis & Cell Counting.*

240 *Gray Value:* We first delineated the MGB across the different ROI's. We then used Fiji's Plot Profile
241 plug-in to output the gray values. Using a custom Python script we then calculated the mean gray values and
242 S.E.M.
243 *Cell Counting:* We used the Cellpose[50] anatomical segmentation algorithm to outline cells in selected
244 sections. We then manually confirmed the masks provided by Cellpose in Fiji using the cell counter plugin.
245 A custom Python script was used to calculate the overlapping masks and percentages.
246
247 *Neural Response Analysis.*
248 Following manual spike sorting, units included in this analysis were selected based on their sound
249 responsive profiles. To select sound-responsive units, we used the find_peaks function from SciPy's Python
250 Library and set the minimum peak height to the mean of the baseline activity–calculated as the average
251 firing rate 50ms prior to tone onset ±3 standard deviations of each unit. If units did not display peaks above
252 this set criteria during the presentation of the tone in light-Off conditions, they were labeled as non-sound
253 responsive units and excluded from further analysis. Spontaneous firing rate was computed as the average
254 firing rate during a time window of 50ms prior to tone onset ($FR_{Spontaneous}$) for both light-Off and light-On
255 trials. Tone-evoked firing rate (FR_{Evoked}) was calculated as the average firing rate for the first 25ms (0-25ms)
256 of the total tone duration (50ms). Late tone-evoked firing rate was calculated ($FR_{EvokedLate}$) was calculated as
257 the average firing rate from 25ms to tone offset (25ms-50ms). Offset responses (FR_{Offset}) were calculated as
258 the average firing rate during a 150ms time-window after tone offset. Light only responses were calculated
259 as the average firing rate during light presentation. We calculated the difference in the response between
260 light-Off and light-On conditions by subtracting the mean normalized firing rate during the first 25ms of
261 tone presentation in the light-Off trials and the mean normalized firing rate during the first 25ms of tone
262 presentation in the light-On trials. To calculate frequency response functions, we averaged the firing rate
263 during early-tone presentation (0-25ms) for all the trials of the individual 19 frequencies in both light-Off
264 and light-On conditions and centered them to their best frequency. Best frequency is defined as the
265 frequency that elicited the highest change in firing rate compared to baseline activity. Linear fits were
266 calculated by using SciKit Learns Linear Regression Model (Python Library) on the mean firing rate of each
267 cell for every repeat of each of the 19 frequencies. Using the outputs of this model, we extracted the slope
268 and the y-intercepts of the fit for each unit's frequency response function.

Statistical Analysis.

We assessed normality of the data using a Shapiro-Wilk tests using Scipy's Stats Python Library. For paired data that violated the assumption of normality, p values were calculated using a Wilcoxon sign-rank tests using Scipy's Stats Python Library. For non-paired data that violated the assumption of normality, p values were calculated using a Wilcoxon rank-sum tests using Scipy's Stats Python Library. The standard error of the mean was used to calculate error bars (±SEM). Symbols: * indicates p values <0.05, ** indicates p values < 0.01, and *** indicates p values <0.001.

Modeling.

Model cells were Hodgkin-Huxley formalism solved by a second order Runge-Kutta ODE solver in MATLAB (ode23, Mathworks). TRN and MGB cells were single-compartment Hodgkin-Huxley models built upon those used previously [51–53] that include T currents. To match the reduced bursting properties in SST^{TRN} and higher-order MGB cells[43,54], those cells had 50% reduced T current densities (0.375 mS/cm^2). Parameters included the following ionic currents and maximal conductances: fast transient Na+ (NaT) 60.5 mS/cm^2, K+ delayed rectifier (Kd) 60 mS/cm^2, K+ transient A (Kt) 5 mS/cm^2, slowly inactivating K+ (K2) 0.5 mS/cm^2, slow anomalous rectifier (AR) 0.025 mS/cm^2, and low threshold transient Ca2+ (CaT) 0.75 mS/cm^2 for PV/MGB cells and 0.375 mS/cm^2 for SST/HO cells. Reversal potentials were 50 mV for sodium, -100 mV for potassium, 125 mV for calcium, -40 mV for AR and -75 mV for leak. Capacitance was 1 μF/cm^2 with leak of 0.1 mS/cm^2. Chemical synapses were modelled as double exponential decay with rise and fall time kinetics of 5 ms and 35 ms respectively, with reversal potentials of 0 mV for excitatory and -100 mV for inhibitory synapses. Electrical synapses were modelled as static coupling conductance of 0.03 mS/cm^2 applied to the voltage difference between the coupled TRN cells, corresponding to a strong electrical coupling (~0.2 coupling coefficient). Tone inputs were simulated as exponentially decaying current pulses (peak amplitude 2.7 μA/cm^2, with decay time constant 30 ms) delivered simultaneously to each of the MGB cells. Each of the TRN cells was inactivated individually through a static conductance of 10 mS/cm^2 and reversal potential of -70 mV for 100 ms during the inputs (**Figure 6B**). Chemical synaptic connections between TRN cells were set at 1 μA/cm^2 for excitatory synapses from MGB to TRN cells, and 3 μA/cm^2 for all inhibitory synapses originating from TRN. For each stimulus condition, we repeated 150 trials under

298 Poisson random noise of 0.2 μA at a rate of 80 Hz for excitatory and 20 Hz for inhibitory events. Among
299 these trials, we varied the percent of trials that included various synaptic connections from TRN cells
300 (**Figure 6C**), in lieu of varying synaptic strengths. Subthreshold current steps of 0.3 μA were applied to all
301 cells to increase excitability. PSTHs were obtained from spike time data histograms with a bin size of 1 ms
302 and smoothed with a 31 ms Hanning window. We normalized each response to the maximum rate in the
303 non-inactivated trial.
304
305
306 ## RESULTS

307 **PV and SST neurons of the TRN project to MGB, targeting different subregions.**

308 MGB is anatomically subdivided into three main subnuclei: the ventral division (vMGB), the medial
309 division (mMGB), and the dorsal division (dMGB). vMGB receives lemniscal projections from the brainstem
310 and provides the most direct auditory input to auditory cortex (AC), whereas dorso-medial geniculate
311 regions provide higher-order information. We first imaged the distribution of PV^{TRN} and SST^{TRN} neuronal
312 projections in MGB using viral neuroanatomical tracing methods. We injected anterograde adeno-
313 associated viruses into the TRN of PV-Cre or SST-Cre mice and traced the axonal projections to the MGB
314 (**Figure 1A & 1C**). We took advantage of the finding that calretinin is solely expressed in the higher-order
315 MGB[55] to characterize the projection patterns of both neuronal subtypes within the MGB. We labeled cell
316 bodies in dorso-medial MGB using calretinin anti-body. The anterograde virus labeled axons in MGB from
317 PV^{TRN} or SST^{TRN} neurons. Whereas PV^{TRN} neurons targeted the central portion of vMGB, SST^{TRN} neurons
318 avoided this region. PV^{TRN} projections were stronger in the central area of ventral MGB rather than
319 peripheral and dorso-medial regions (**Figure 1B;** *$N = 14$ ROIs, $p \leq 0.001$, signed-rank test*). By contrast,
320 projections of SST^{TRN} targeted the dorsal and medial MGB (**Figure 1D;** *$N = 8$ ROIs, $p = .023$, signed-rank*
321 *test*). Combined, these data demonstrate that PV^{TRN} and SST^{TRN} neurons exhibit differential projection
322 patterns to the MGB.
323

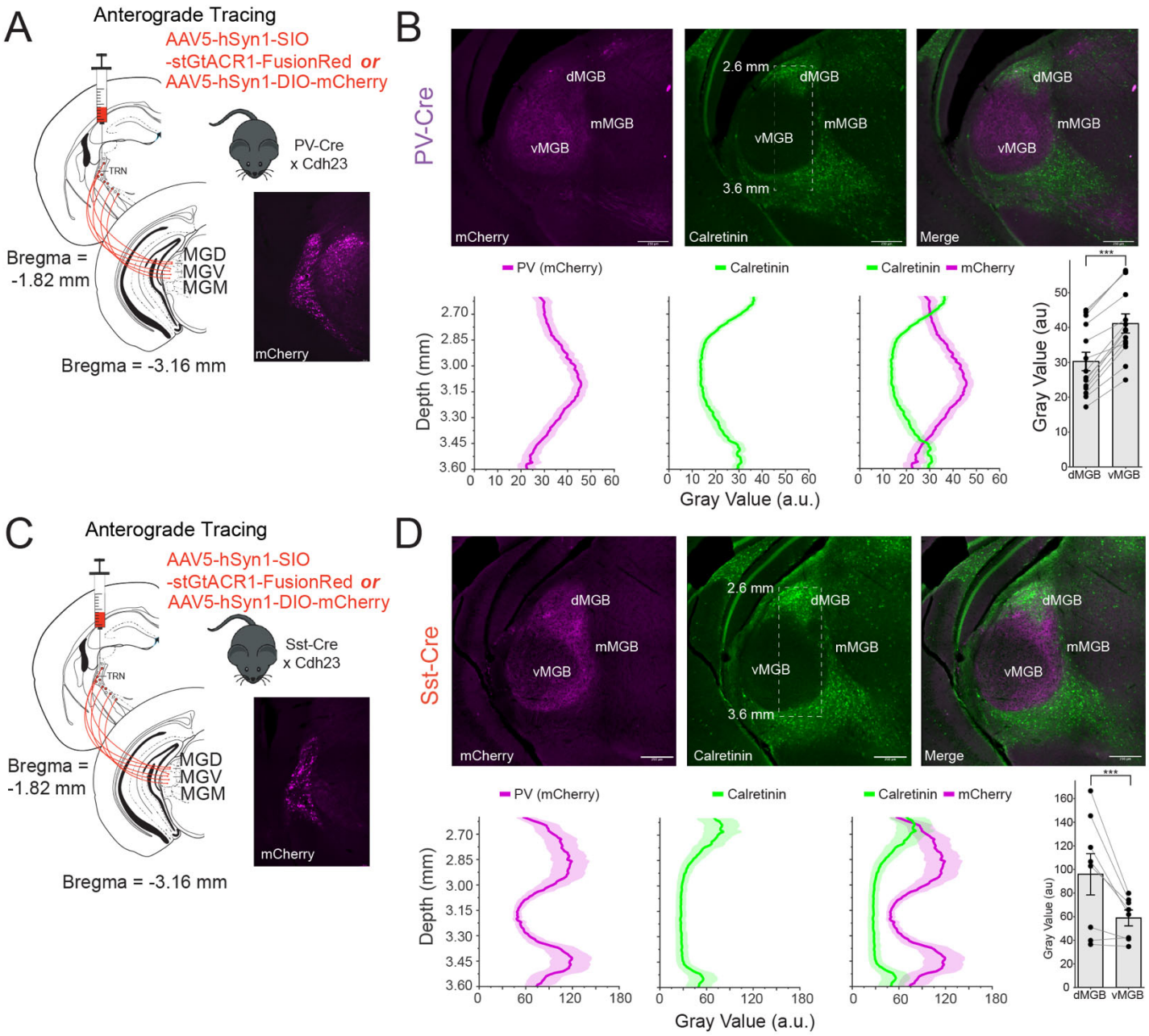

Figure 1. PV^{TRN} and SST^{TRN} project to different subregions of the MGB. A. Experimental design for anatomical experiments. PV-cre mice were injected with AAV5-hSyn1-DIO-mCherry into TRN for anterograde tracing of PV neurons in the TRN. Inset: mCherry expression in the TRN indicating the localization of the virus. **B. Top**: Projections of PV^{TRN} neurons primarily target the ventral subdivision of the MGB. *Left panel*: Viral expression of projections to the MGB (magenta). *Middle panel*: Immunohistochemical labeling of calretinin in the MGB (green). *Right panel*: Merged channels. **Bottom**: Quantification of the fluorescence intensity of projections from PV^{TRN} neurons that target MGB (Dashed box in top middle panel outlining the ROI). *Left panel*: intensity of viral expression of projections to the MGB in the ROI along the dorso-ventral axis. Dashed lines indicate extent of vMGB. *Middle panel*: intensity of the immunohistochemical labeling of calretinin in the MGB in the ROI along the dorso-ventral axis. *Right panel*: merged channels. *Barplot:* mean intensity of the projections of PV-audTRN neurons in dorsal and ventral MGB (N =14 ROIs; n = 3 mice). **C.** SST-cre mice were injected with AAV5-hSyn1-DIO-mCherry into TRN for anterograde tracing of SST neurons in the TRN. **D. Top**: Projections of SST^{TRN} neurons primarily avoid the ventral subdivision of the MGB. *Left panel*: Viral expression of projections to the MGB (magenta). *Middle panel*: Immunohistochemical labeling of calretinin in the MGB (green). *Right panel*: Merged channels. **Bottom**: Quantification of the fluorescence intensity of projections from SST^{TRN} neurons that target MGB (Dashed box in top middle panel outlining the ROI). *Left panel*: intensity of viral expression of

342 projections to the MGB in the ROI along the dorso-ventral axis. *Middle panel*: intensity of the
343 immunohistochemical labeling of calretinin in the MGB in the ROI along the dorso-ventral axis. *Right panel*:
344 merged channels. *Barplot:* mean intensity of the projections of PV-audTRN neurons in dorsal and ventral
345 MGB (N =8 ROIs; n = 3 mice). *Scale bar = 0.25 mm. vMGB: ventral MGB; dMGB: dorsal MGB; mMGB:*
346 *medial MGB; White dashed box in the top middle panel indicates ROI for fluorescence intensity*
347 *quantification.*
348

349 **Inactivation of PV^{TRN} and SST^{TRN} neurons differentially affects tone-evoked responses in the**
350 **MGB.**

351 Because of our anatomical results and previous work identifying genetically distinct TRN neurons
352 that express different anatomical and physiological properties[42,43], we next tested whether and how MGB
353 neurons are modulated by PV^{TRN} and SST^{TRN} neurons. We inactivated SST and PV neurons in audTRN
354 during tone-evoked responses in MGB neurons. We injected a Cre-dependent soma-targeted inhibitory
355 opsin (AAV5-hSyn-SIO-stGtACR1-FusionRed) in the audTRN of SST-Cre or PV-Cre mice (**Figure 2A-B,**
356 **2G-H**). This virus only expresses in the soma of Cre-expressing neurons, reducing the chance of effects from
357 backpropagating action potentials from local terminals[56]. We verified that the virus expression was
358 restricted to the appropriate cell type (**Supplementary Figure S1**). We then implanted an optic fiber
359 above audTRN, a headpost, and a ground pin for awake *in-vivo* electrophysiological recordings. In our
360 experiments, mice passively listened to tones ranging from 3-80kHz, while we recorded and measured the
361 spiking activity of MGB neurons. We quantified neuronal firing rate for both light-off and light-on conditions
362 and calculated the difference between these conditions as a function of probe depth within the MGB (**Figure**
363 **2D-F, 2I-K**). To confirm that our optogenetic manipulations indeed inhibited audTRN neurons, in a
364 separate set of experiments, shining light over the TRN suppressed tone-evoked neuronal activity in neurons
365 recorded in TRN (**Supplementary Figure S2**). We have separately verified in slices that shining light over
366 the TRN resulted in silencing of a neuron expressing stGtACR1 (**Supplementary Figure S3**).

367 We expected that PV^{TRN} neuronal inactivation would drive the disinhibition of responses of MGB
368 neurons, which would be stronger in the central vMGB. By contrast, we expected that inactivating SST^{TRN}
369 neurons would suppress MGB responses to sounds via a double inhibitory pathway. Because SST^{TRN} and
370 PV^{TRN} are reciprocally connected, inactivating SSTs could disinhibit PVs which would in turn suppress MGB
371 neurons. This effect would be stronger in the central regions of MGB, and there would be mixed effects in
372 the dorsal regions of the MGB.

373 Indeed, inhibiting PV^{TRN} neurons facilitated sound-evoked responses in a large fraction of MGB
374 neurons (**Figure 2D-F**). The facilitation was stronger for the central regions of MGB than dorsal MGB (p =
375 *0.0070, binned by depth: 2.5-2.9mm versus 3.1-3.5 mm, rank-sum test*), and this change was exacerbated
376 by the larger number of facilitated neurons in center (**Figure 2F**). Surprisingly, there was also a strong
377 suppression of a fraction of neurons throughout MGB. However, this suppression was not differential across
378 the depth of MGB (p = *0.18, rank-sum test)*. Inactivating SST^{TRN} neurons resulted in a dominant suppression
379 of tone-evoked responses in MGB, with a handful of neurons exhibiting facilitation (**Figure 2I-K**).
380 Furthermore, the suppression was stronger in the dorsal MGB as compared to vMGB (p = *0.000050, rank-*
381 *sum test*). These results suggest that PV neurons provide direct inhibition to MGB, while SST neurons
382 disinhibit the thalamocortical auditory pathway.

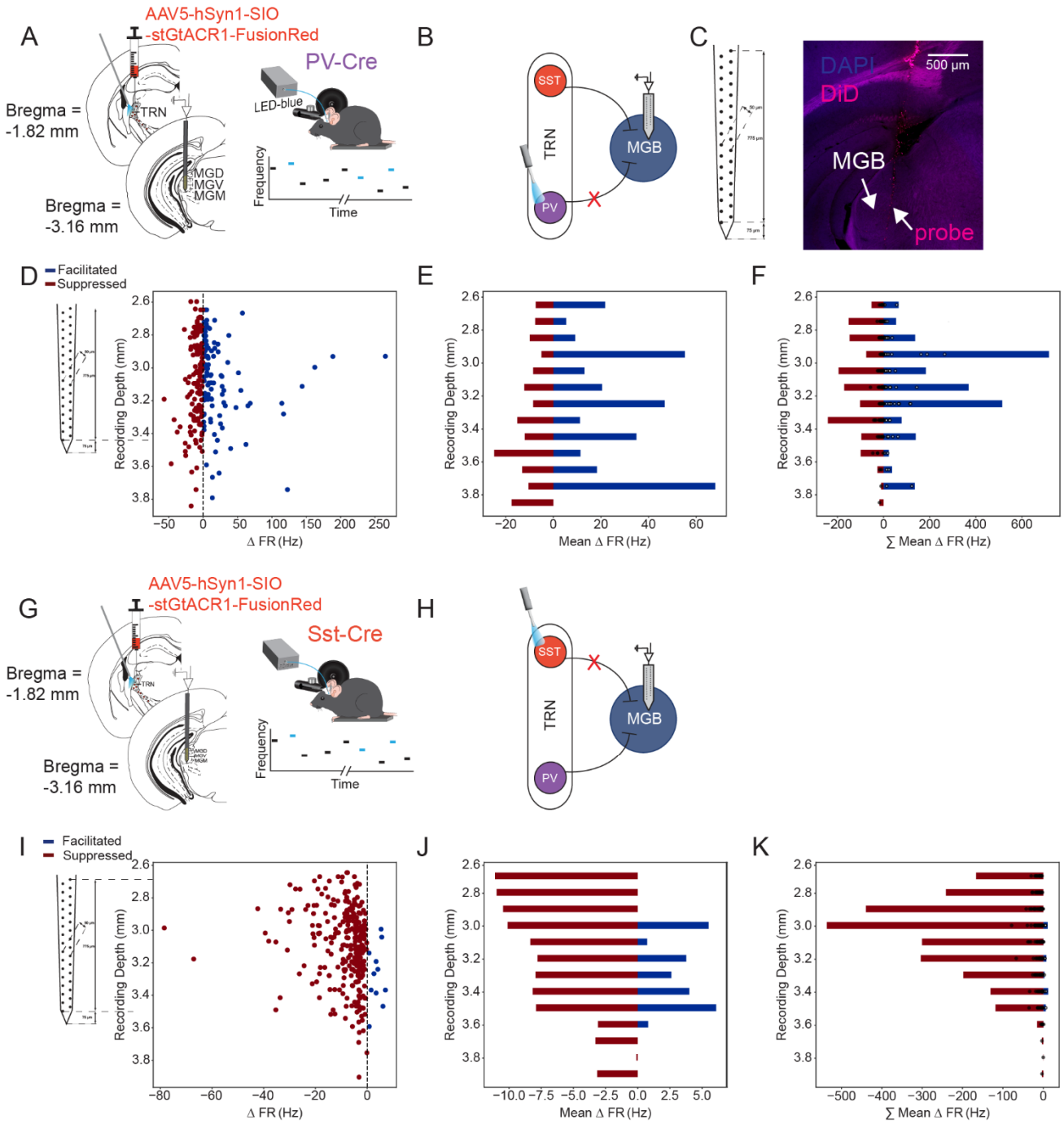

Figure 2. Inactivation of PV^{TRN} and SST^{TRN} neurons differentially affect tone-evoked activity in MGB neurons. A. PV mice were injected with a soma-targeted AAV5-hSyn1-DIO-stGtACR1-FusionRed into the audTRN and were implanted with an optic fiber. We recorded from MGB neurons in awake head-fixed mice. We presented a set of pure tones in light-on and light-off conditions. **B.** We selectively inactivated PV neurons of the audTRN while recording from neurons in the MGB using a vertical multi-channel electrode that spanned the depth of dMGB and vMGB, with the top electrode positioned at the tip of dMGB. **C.** Example probe track labeled using DiD (magenta), from a recording in MGB. **D.** Scatter plot showing the change in firing rate (FR) of recorded MGB neurons with PV^{TRN} inactivation as a function of probe depth. Red: suppressed neurons; Blue: facilitated neurons. **E.** Mean change in FR of recorded MGB neurons with PV^{TRN} inactivation as a function of probe depth in 100 µm bins. **F.** Total change in FR of recorded MGB neurons with PV^{TRN} inactivation as a function of probe depth in 100 µm bins. **G-K.** Same as **A-B, D-F**, but for SST^{TRN} inactivation. (N (PV) =239, n = 4 mice. N (SST): 282, n = 4 mice). ROIs; n = 3 mice). *Scale bar = 0.25 mm. vMGB: ventral MGB; dMGB: dorsal MGB; mMGB: medial MGB; White dashed box in the top middle panel indicates ROI for fluorescence intensity quantification.*

399 **Inactivation of PV^{TRN} neurons facilitates or suppresses tone-evoked responses in MGB.**

400 We next examined in more detail the effect of inactivating PV^{TRN} neurons on tone-evoked responses
401 in MGB. For a representative *facilitated* MGB neuron, the raster plots and peri-stimulus time histogram
402 (PSTH) (**Figure 3A-B**) demonstrate an increase in activity during tone presentation. For this neuron, the
403 increase was more pronounced 0-25 ms after stimulus onset and affected the responses across tone
404 frequencies (**Figure 3C**). The effects subsided 25-50 ms after stimulus onset (**Figure 3D**). For a
405 representative *suppressed* MGB neuron, the raster plot and PSTH depict a reduction in spiking activity
406 during the tone (**Figure 3E-F**). The suppressive effects of PV^{TRN} inactivation were more pronounced 0-25
407 ms (**Figure 3G**) but persisted 25-50 ms after tone onset (**Figure 3H**).

408 Across the population of MGB neurons, during tone presentation, 35% of neurons were facilitated,
409 48% of neurons were suppressed and 17% of neurons in the MGB were not affected due to PV^{TRN} inactivation
410 (**Figure 3I**). Facilitated neurons demonstrated a sharp peak followed by a prolonged decay in firing rate
411 after tone onset and in the absence of a tone (**Figure 3J**). Similarly, for suppressed neurons, the effect of
412 the light in the absence of tone was prolonged, and with tone resulted in an overall decrease in peak tone-
413 evoked response followed by a reduction in activity (**Figure 3K**). Over the population, there was no
414 significant effect during spontaneous activity prior to sound and light stimulus on no-light and light-on trials
415 (**Figure 3M**). In the tone condition, neuronal activity was significantly facilitated or suppressed both in the
416 beginning (0-25 ms) and during the second half (25-50 ms) of the tone duration (**Figure 3N-O;** *N*
417 *(facilitated): 101, N (suppressed): 138; p (facilitated-0-25ms)* $\leq$ *0.001, p (suppressed-0-25ms)* $\leq$ *0.001; p*
418 *(facilitated-25-50ms)* $\leq$ *0.001, p (suppressed-25-50ms)* $\leq$ *0.001; signed-rank test*). When PV^{TRN} neurons
419 were inactivated, time-to-peak significantly increased in the facilitated MGB neurons and slightly decreased
420 in the suppressed MGB neurons (**Figure 3L;** *N (facilitated): 101, N (suppressed): 138; p (facilitated-0-*
421 *25ms)* $\leq$ *0.001, p (suppressed-0-25ms)* $\leq$ *0.017; signed-rank test*). This suggests that PVs selectively control
422 time-to-peak in neuronal responses in MGB. We confirmed that the light presentation alone did not affect
423 the neuronal firing rate by repeating the experiments after injecting a virus encoding only the fluorescent
424 reporter without the opsin (**Supplementary Figure S4**) and found no effect of light on spontaneous or
425 tone-evoked responses in MGB. Overall, these results demonstrate that inactivating PV^{TRN} neurons rapidly
426 affected tone-evoked responses in MGB, with effects persisting over the stimulus duration. In addition, we
427 found that PV^{TRN} neurons can both directly suppress neuronal responses in MGB and enhance the response

428 firing rate indicating that these neurons may be involved in multiple mechanisms that shape MGB firing
429 rates.

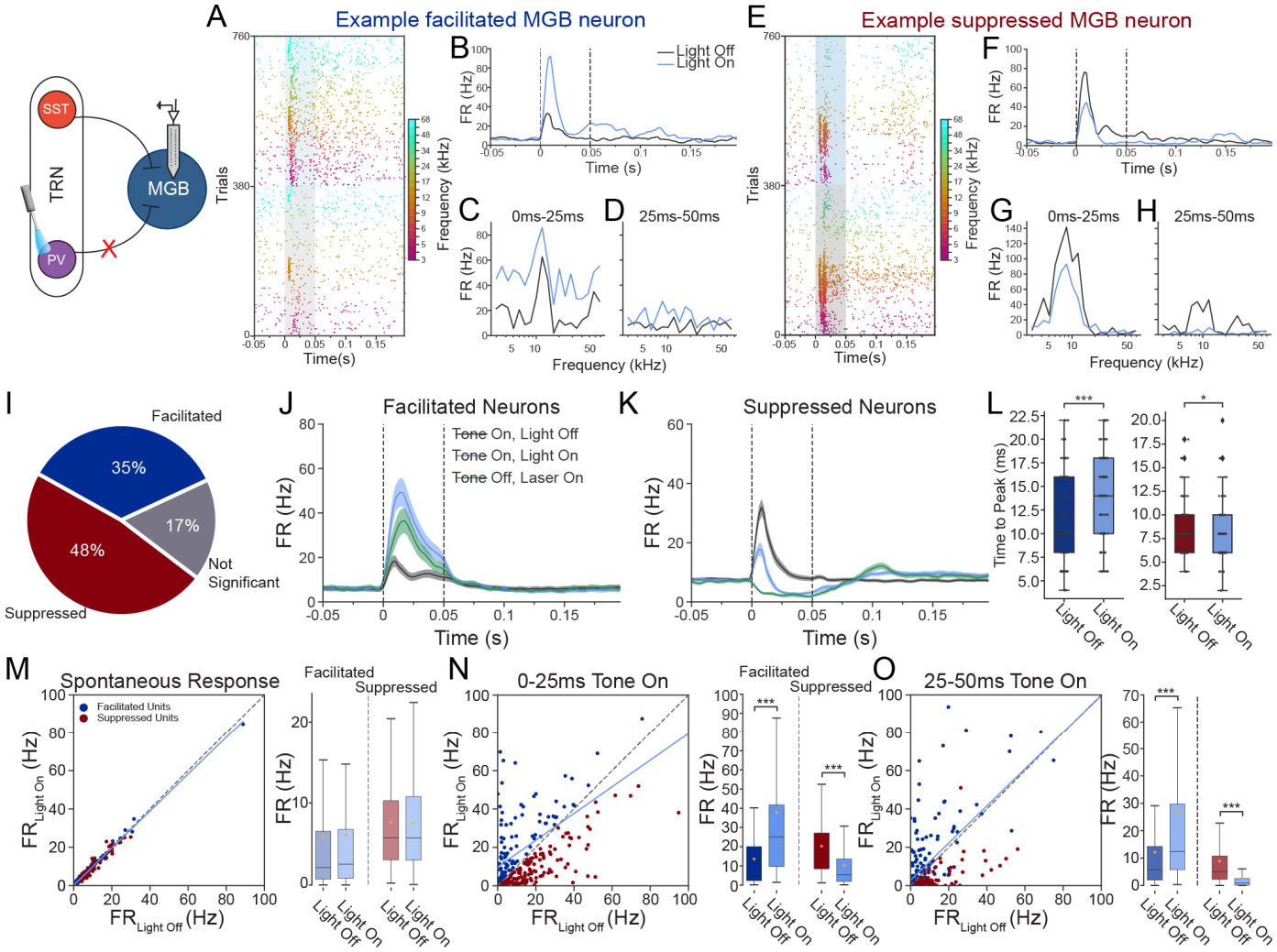

430

431 **Figure 3. Inactivation of PV^{TRN} neurons facilitates and suppresses tone-evoked activity in**
432 **MGB neurons. A.** PV mice were injected with a soma-targeted AAV5-hSyn1-DIO-stGtACR1-FusionRed
433 into the audTRN and were implanted with an optic fiber. We recorded from MGB neurons in awake head-
434 fixed mice. We presented a set of pure tones in light-on and light-off conditions. We selectively inactivated
435 PV^{TRN} neurons while recording from neurons in MGB. Raster plot of an example facilitated unit; trials are
436 ordered by frequency and light condition. The gray box indicates light off conditions, blue box indicating the
437 light on conditions. **B.** PSTH of the facilitated example unit averaged across all trials for the light off (black
438 line) and light on (blue line) conditions. **C.** Frequency response function for the facilitated unit during the
439 first 25ms of tone presentation during light off and light on conditions. **D.** Frequency response function of
440 the unit during the late 25-50ms of tone presentation. **E-H.** same as A-D, but for a representative facilitated
441 neuron. **I.** Pie chart breaking down the effect of PV^{TRN} inactivation in neurons of the MGB. We find that
442 48% of recorded units had suppressed tone-evoked responses (red slice), 35% of recorded units had
443 facilitated tone-evoked responses (navy blue slice), and 17% of tone-responsive units were not affected by
444 light manipulation (gray slice). **J,K.** Mean PSTH of facilitated (J) and suppressed (K) recorded neurons in
445 MGB (N = 101 facilitated. N = 138 suppressed). Light-only trials (green line), tone-only trials (black line),
446 and tone- and light-on trials (light blue line). **L.** Time to peak of tone-evoked responses for facilitated (left,
447 blue) and suppressed (right, red) MGB neurons for light off (blue/red) and light on (light blue) trials. **M-O.**
448 Left: scatter plot, and right: box plot and boxplot of the mean FR for light off and light on conditions for
449 facilitated (blue) and suppressed (red) neurons during spontaneous activity (**M**), 0-25 ms post stimulus

450 onset (**N**), and 25-50 ms post stimulus onset (**O**). N = 239; n = 4. Shaded areas represent SEM±. Error bars
451 represent SEM±. *** denotes p-value < 0.001; * denotes p-value < 0.05.
452

453 **Inactivation of SST^{TRN} neurons primarily suppresses tone-evoked responses of MGB**
454 **neurons.**

455 We next examined in more detail the effect of inactivating SST^{TRN} neurons on tone-evoked responses
456 of MGB neurons. For a representative facilitated MGB neuron, the raster plots and post-stimulus time
457 histograms (**Figure 4A-B**) demonstrate an increase in activity at the onset of tone presentation. For this
458 neuron, the increase was present 0-25 ms after stimulus onset and affected the responses to frequencies
459 near the neuron's best frequency (**Figure 4C**). The effects were not apparent in the 25-50 ms tone bin
460 (**Figure 4D**). For a representative suppressed MGB neuron, the raster plot and PSTH depict a reduction in
461 spiking activity throughout the tone (**Figure 4E-F**). The suppressive effects were more pronounced 0-25
462 ms after tone onset (**Figure 4G-H**).

463 Across the population of neurons, during tone presentation, 78% neurons were suppressed, only 3%
464 of neurons were facilitated and 19% of neurons in the MGB were not affected by SST^{TRN} inactivation (**Figure**
465 **4I**). The average PSTH across the few facilitated neurons (N = 11 neurons) shows barely detectable
466 amplification (**Figure 4J**). For suppressed neurons, suppression driven by SST^{TRN} neuronal inactivation
467 was prolonged in the absence of tone. In the presence of a tone, the tone-evoked response was reduced and
468 shortened (**Figure 4K**). Over the population, there was no significant effect during spontaneous activity on
469 light-on versus light-off trials prior to stimulus (**Figure 4M**). Temporally, neuronal activity was
470 significantly suppressed both in the beginning (0-25 ms) and during the second half (25-50 ms) of the tone
471 presentation (**Figure 4N-O;** *N (facilitated): 11, N (suppressed): 271; p (facilitated-0-25ms) = 0.001, p*
472 *(suppressed-0-25ms) ≤ 0.001; p (facilitated-25-50ms) ≤ 0.147, p (suppressed-25-50ms) ≤ 0.001; signed-*
473 *rank test*), although some cells, initially suppressed, exhibited facilitation in the second half of the tone.
474 Unlike for PV^{TRN} suppression, there was no change in the time-to-peak response of facilitated MGB neurons,
475 and a small decrease for suppressed MGB neurons, upon inactivation of SST^{TRN} neurons (**Figure 4L;** *N*
476 *(facilitated): 11, N (suppressed): 271; p (facilitated-0-25ms) = 0.461, p (suppressed-0-25ms) = 0.003;*
477 *signed-rank test*). We confirmed that the effects of light presentation alone did not affect the neuronal firing
478 rate by repeating the experiments but injecting a virus encoding only the fluorescent reporter, and not the

opsin (**Supplementary Figure S5**). Overall, these results demonstrate that inactivating SST^{TRN} neurons largely drove a suppression of MGB neurons.

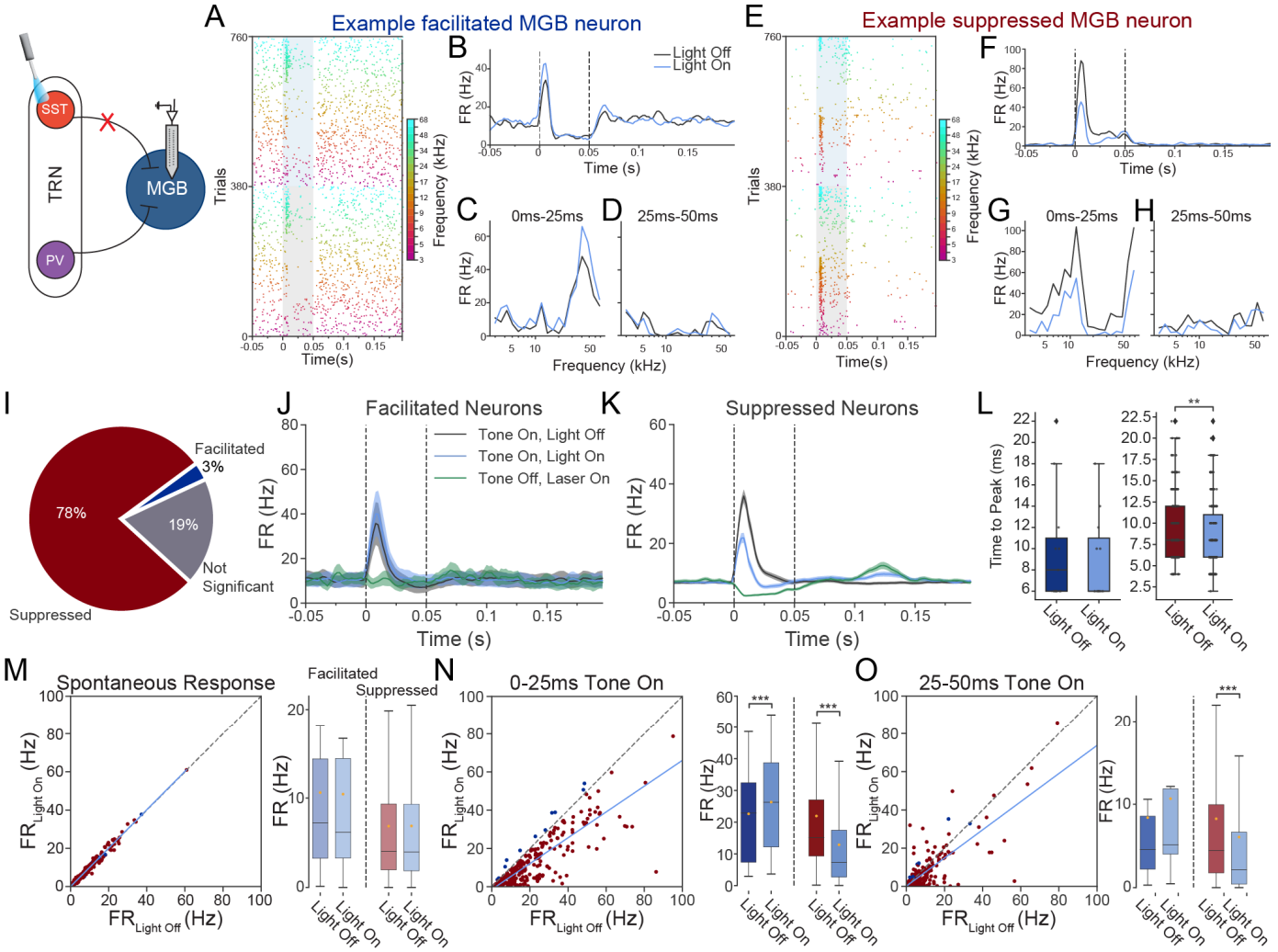

Figure 4. Inactivation of SST^{TRN} neurons predominantly suppresses tone-evoked activity in MGB neurons. A. SST mice were injected with a soma-targeted AAV5-hSyn1-DIO-stGtACR1-FusionRed into the audTRN and were implanted with an optic fiber. We recorded from MGB neurons in awake head-fixed mice. We presented a set of pure tones in light-on and light-off conditions. We selectively inactivated SST^{TRN} neurons while recording from neurons in MGB. Raster plot of an example facilitated unit; trials are ordered by frequency and light condition. The gray box indicates light off conditions, blue box indicating the light on conditions. **B.** PSTH of the facilitated example unit averaged across all trials for the light off (black line) and light on (blue line) conditions. **C.** Frequency response function for the facilitated unit during the first 25ms of tone presentation during light off and light on conditions. **D.** Frequency response function of the unit during the late 25-50ms of tone presentation. **E-H.** same as A-D, but for a representative facilitated neuron. **I.** Pie chart breaking down the effect of SST^{TRN} inactivation in neurons of the MGB. We find that 78% of recorded units had suppressed tone-evoked responses (red slice), 3% of recorded units had facilitated tone-evoked responses (navy blue slice), and 19% of tone-responsive units were not affected by light manipulation (gray slice). **J,K.** Mean PSTH of facilitated (J) and suppressed (K) recorded neurons in MGB (N = 11 facilitated. N = 271 suppressed). Light-only trials (green line), tone-only trials (black line), and tone- and light-on trials (light blue line). **L.** Time to peak of tone-evoked responses for facilitated (left, blue) and suppressed (right, red) MGB neurons for light off (blue/red) and light on (light blue) trials. **M-O.** Left: scatter plot, and right: box plot and boxplot of the mean FR for light off and light on conditions for facilitated (blue) and suppressed (red) neurons during spontaneous activity (**M**), 0-25 ms post stimulus onset (**N**), and 25-50 ms post stimulus onset (**O**). N = 282; n = 4. Shaded areas represent SEM±. Error bars represent SEM±. *** denotes p-value < 0.001; * denotes p-value < 0.05.

504

505 **PV^{TRN} and SST^{TRN} differentially affect frequency tuning of MGB neurons.**

506 Inactivation of PV^{TRN} neurons produced significant changes in MGB tuning for both the facilitated-
507 and suppressed-tone evoked activity groups; with a significant shift upwards and a significant shift
508 downwards in the frequency response function, respectively (**Figure 5A-B;** *N (facilitated): 101, N =*
509 *(suppressed): 138; p (facilitated-all octaves) ≤ 0.001, p (suppressed-all octaves) ≤ 0.001; signed-rank test*).
510 Interestingly, in facilitated MGB neurons, response to best frequency increased less strongly than the
511 response to the sideband frequencies (**Figure 5A;** *N (facilitated) = 101, N (suppressed) = 138; p*
512 *(facilitated- sidebands) ≤ 0.001, p (facilitated-best frequency) = 0.204; signed-rank test*). To examine
513 frequency selectivity of neurons– or how specific neuronal responses are to a particular frequency–we
514 calculated the sparseness index. A value closer to 1 indicates that the unit responds narrowly to a set of
515 stimuli and a value closer to 0 indicates that units will respond to a broader range of stimuli. We found that
516 inactivation of PV^{TRN} significantly affected sparseness in both subgroups. Following of PV^{TRN} inactivation,
517 sparseness in facilitated MGB neurons significantly decreased, indicating that neurons became more broadly
518 tuned (**Figure 5A;** *N (facilitated): 101; p (both time points) ≤ 0.001; signed-rank test*). Interestingly, in
519 suppressed MGB neurons, PV inactivation increased sparseness, indicating that neurons on average became
520 more narrowly tuned (**Figure 5B;** *N (suppressed): 138; p (both time points) ≤ 0.001; signed-rank test*).
521 These results indicate that of PV^{TRN} neurons contribute to how narrowly or broadly tuned MGB neurons are
522 to auditory stimuli.

523 Because PV^{TRN} neurons affect frequency tuning of MGB neurons, we asked whether the observed
524 effects of PV^{TRN} inactivation depended on whether the MGB recording site(s) were tonotopically organized
525 along the probe depth (dorsal-ventral axis). To test this, we separately analyzed and compared tonotopic
526 versus non-tonotopic MGB recordings. We found that PV^{TRN} inactivation produced similar effects on MGB
527 sound responses, regardless of recording site tonotopy (**Supplementary Figure S6**).

528 Inhibition of SST^{TRN} neurons produced no significant changes in tuning for the few MGB neurons
529 that had facilitated tone-evoked responses (**Figure 5C;** *N (facilitated): 11; p (0-25ms) ≥ 0.05; signed-rank*
530 *test*). However, MGB neurons that had suppressed tone-evoked firing rates show a significant downward
531 shift in the frequency response function during the first 25ms of the tone presentation and the remaining

532 25ms of tone presentation (**Figure 5D;** *N = (suppressed): 271; p (both time points) ≤ 0.05; signed-rank*
533 *test*). We found that inactivation of SST^{TRN} neurons did not affect sparseness in the facilitated group *(***Figure**
534 **5C***; N (facilitated): 11; p (0-25ms) = 0.638*; *p (25-50ms) = 0.765*; *signed-rank test*). However, the
535 sparseness index in the suppressed group of neurons was significantly increased during SST^{TRN} inactivation
536 (**Figure 5D;** *N (suppressed): 101; p (both time points) ≤ 0.001; signed-rank test*). Similar to inactivation
537 of PV^{TRN} neurons, we again found that SST^{TRN} inactivation produced similar effects on MGB sound
538 responses, regardless of recording site tonotopy (**Supplementary Figure S7**). Together, these results
539 indicate that SST neurons of the TRN contribute to how narrowly or broadly tuned MGB neurons are to
540 auditory stimuli.
541

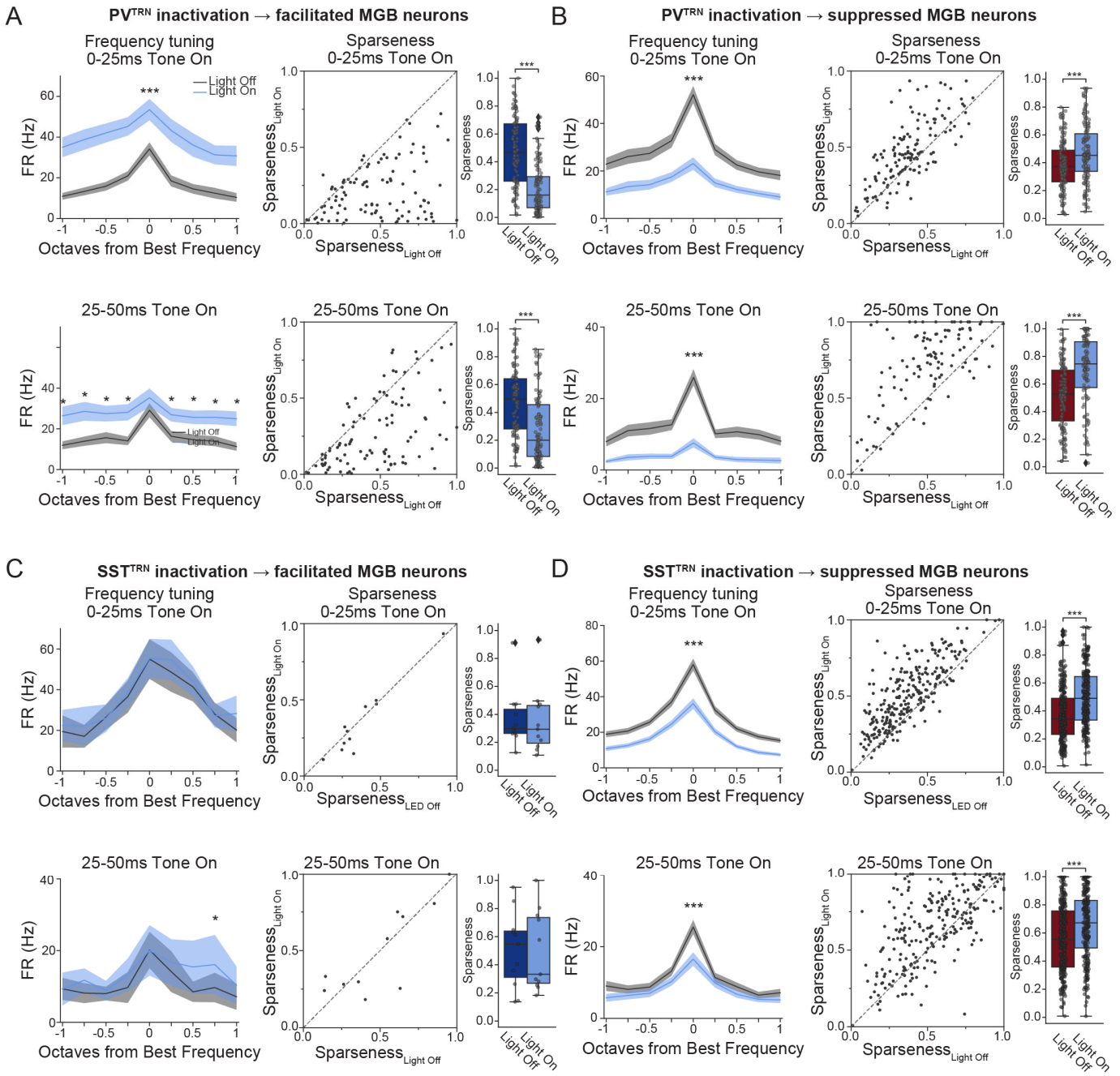

Figure 5. Inactivation of PV^{TRN} and SST^{TRN} neurons differentially affect frequency tuning of MGB neurons. A-D. *Left:* Mean frequency response function for light on (light blue) and light off (light gray) trials for neurons centered on best frequency (0 octaves = BF). Shaded areas represent SEM±. *Right*. Scatterplot and bar plot of sparseness. Error bars represent SEM±. **A, C.** Facilitated neurons. **B, D.** Suppressed neurons. **Top:** 0-25 ms post stimulus onset. **Bottom:** 25-50 ms post stimulus onset. N = 239 neurons; n = 4 mice (PV). N = 282 neurons; n =4 mice (SST). *** denotes p-value < 0.001; * denotes p-value < 0.05.

551 **Specifics of connectivity between MGB-TRN circuits determine the sign of MGB responses**
552 **during TRN cell-type inactivation.**
553
554 To examine the many possible connectivity schemes of primary and higher-order auditory
555 thalamocortical circuits that may account for the observed changes in sensory responses during inactivation
556 of specific TRN populations, we constructed a 4-cell Hodgkin-Huxley model (see Methods) comprising two
557 channels: a primary vMGB relay cell reciprocally connected to a PV^{TRN} cell, and a higher-order MGB cell
558 reciprocally connected to a SST^{TRN} cell (**Figure 6A-B**), matching the subtype-specific connections that we
559 identified and have been previously demonstrated for other sensory modalities[42,43]. Without connectivity
560 between primary and higher-order channels, inactivation of the PV^{TRN} cell always allowed substantially
561 increased responses in the vMGB firing rate to a tone input, whereas inhibiting the SST^{TRN} cell has no effect
562 at all on vMGB response, as expected (not shown). Those trials served as a comparison control for
563 subsequent trials.
564 We first examined whether intra-TRN connectivity would suffice to produce both suppression and
565 facilitation of vMGB responses during cell type-specific silencing (**Figure 3-4**). Electrical synapses
566 extensively couple TRN cells, including coupling between subtypes[45], that may substantially modulate
567 activity within the thalamocortical circuits examined here[52,57]. We examined the effect of inter-type TRN
568 coupling, using a strong electrical synapse with coupling coefficient ~0.2, on the responses of the primary
569 MGB cell. Similar to the uncoupled control case, vMGB responses were facilitated when PV^{TRN} was
570 inactivated (**Figure 6D**, left), and once again as expected we saw no changes in vMGB responses during
571 inactivation of SST^{TRN} (**Figure 6D, right**). Although the existence of inhibitory synapses between TRN
572 neurons in mature tissue has been controversial [58], there is some evidence for lateral inhibition within
573 TRN[59,60]. Inclusion of a lateral inhibitory synapse from SST^{TRN} to PV^{TRN} allowed a facilitated vMGB response
574 during PV^{TRN} inactivation, and we noted that MGB responses during no-inactivation trials were also elevated
575 from the control response (**Figure 6E, left**). Silencing SST^{TRN} cells in this circuit produced a substantial
576 reduction in the tone response of the vMGB neuron compared to control responses (**Figure 6E, right**),
577 matching the experimental results (**Figure 2, 4**) through relief of disynaptic inhibition. Silencing either cell
578 type in a circuit that included inhibitory connections from PV^{TRN} to SST^{TRN} did not reduce tone responses of
579 vMGB, however (not shown). Thus, one specific form of intra-TRN connectivity, from SST^{TRN} to PV^{TRN} cells,

580 is a candidate circuit mechanism underlying the unexpected suppression of MGB during cell type-specific
581 TRN inactivation.

582 We then asked whether the relative strengths of within-TRN, lateral inhibition and TRN-MGB
583 reciprocal inhibition could control the sign of vMGB responses during selective silencing, as we anticipate
584 that in real tissue, mixes of connectivity and strength will co-exist within a spectrum across these various
585 schemes. To test the effect of heterogeneous circuitry on firing rate changes in primary vMGB cells, we varied
586 the ratio of lateralization within the circuits over a set of trials. In circuits where TRN and MGB are
587 reciprocally connected, varied relative strengths of lateral intra-TRN inhibition always produce facilitation
588 of vMGB responses when PV^{TRN} is inactivated (**Figure 6F, left**); the effect of SST^{TRN} lateralization was only
589 to modulate the total facilitation produced. During SST^{TRN} inactivation, increases in SST^{TRN} lateral inhibition
590 suppressed MGB responses independently of the presence of PV^{TRN} lateral inhibitory synapses (**Figure 6F,**
591 **top right**). We note that the addition of coupling between TRN cells allowed for bidirectionality in changes
592 in vMGB rate when SST^{TRN} was inactivated, for networks with weak SST-to-PV lateralization (**Figure 6F,**
593 **bottom right**). From this set of simulations addressing intra-TRN connectivity, we conclude that
594 inactivating SST^{TRN} can reproduce the unexpected suppression of vMGB response when SST-to-PV synapses
595 or gap junctions are included; however, lateral intra-TRN connections alone cannot reproduce the
596 bidirectional effects of PV^{TRN} inactivation.

597 Next, we asked whether the responses of primary vMGB might change during cell type-specific
598 inactivation in the context of variations in feedback inhibition. TRN cells send divergent inhibitory
599 connections to several MGB cells but often do not send inhibition back to the same cell that excite them[61,62].
600 Additionally, activation of one thalamic nucleus can produce inhibition in nearby sensory-related nuclei (i.e.
601 activation of POM evoking IPSCs at VPM) thought to arise from TRN[63,64]. Thus, we included and varied the
602 amount of divergent feedback inhibition from TRN to MGB in our circuits. When inactivating PV^{TRN} cells,
603 inclusion of both reciprocal and divergent inhibitory feedback still produced facilitation of the vMGB
604 response (**Figure 6G, left**). For inactivation of SST^{TRN} cells in the context of divergent inhibition, vMGB
605 responses were facilitated when circuits contained both reciprocal and divergent inhibitory synapses
606 (**Figure 6G, right**). In circuits with only divergent but lacking reciprocal inhibitory feedback, PV^{TRN}
607 inactivation produced a suppression of vMGB response (**Figure 6H, left**). Thus, inclusion of divergent
608 feedback is a candidate circuit for reproducing the experimental results of PV^{TRN} inactivation. In circuits

609 with only divergent inhibitory feedback from TRN to MGB cells, SST^{TRN} inactivation produced greater
610 facilitation of vMGB responses (**Figure 6H, right**). Thus, we conclude that uniformly divergent feedback
611 inhibition is unlikely to account for the experimental observations of vMGB suppression during SST^{TRN}
612 inactivation.

613 Finally, we asked if variations in the relative power of the two types of feedback inhibition, combined,
614 could allow both vMGB enhancement and suppression during cell type-specific inactivation trials.
615 Increasing the relative strength of the divergent inhibitory synapses decreased the responses of the vMGB
616 cell, while increasing the strength of reciprocal inhibition increased those responses, during PV^{TRN}
617 inactivation trials compared to the baseline firing rate (**Figure 6I, top left**). This is consistent with the
618 bidirectionality of the experimental results for PV^{TRN} inactivation (**Figure 3**). SST^{TRN} inactivation produced
619 only increases in vMGB activity, as divergent inhibitory ratio increased from zero (**Figure 6I, top left**),
620 inconsistent with experiments. However, electrical coupling added to this circuitry allowed SST^{TRN}
621 inactivation to diminish vMGB responses for weakly lateralized networks (**Figure 6I, middle**). Including
622 SST^{TRN}-to-PV^{TRN} lateral inhibition in this case modulated the SST^{TRN} inactivation response towards more
623 suppressed outcomes (**Figure 6I, bottom right).** Together, our simulations lead us to conclude that
624 divergent feedback connections, together with electrical synapses or SST^{TRN}-to-PV^{TRN} inhibition, may be
625 embedded within the thalamus and serve as the sources of the bidirectional vMGB responses observed
626 during PV^{TRN} inactivation and the suppression during SST^{TRN} inactivation.

627

628

629

630

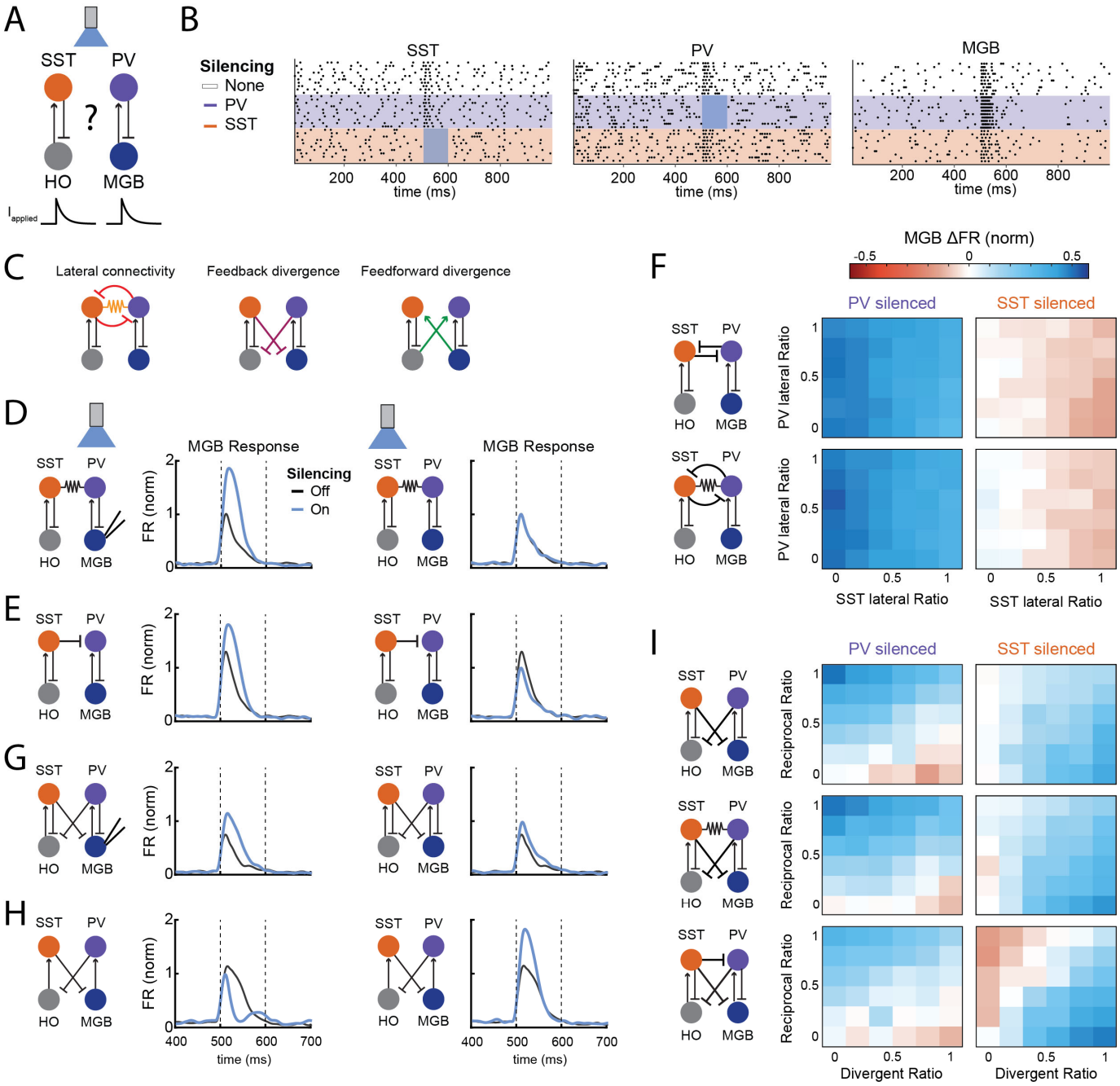

Figure 6. Schemes of circuit connectivity that account for bidirectional modulation of vMGB responses during subtype-specific inactivation in TRN. A. 4-cell model of primary sensory MGB-TRN pairs and higher order (HO) MGB-TRN pairs. **B.** Raster plots from trials with no inactivation, during PV inactivation (purple) and during SST^{TRN} inactivation (orange). **C.** Candidate connectivity schemes tested in models. **D.** PSTH of MGB firing for circuits with electrical coupling between TRN subtypes. MGB responses are normalized to the peak response during non-inactivated trials for no connectivity between columns. Left, primary MGB firing rate to input alone (black line) and with PV^{TRN} silencing (light blue line). Right, MGB firing rate input alone (black line) and with SST^{TRN} silencing (light blue line). **E**. As in D, for a circuit including lateral SST^{TRN} to PV^{TRN} connections. **F**. Effect of inactivation on MGB rate for heterogeneous combinations of lateral inhibitory connections, with and without electrical synapses between TRN cells. The ratio of lateral synapses is the percent of trials that included lateral synapses for each TRN cell type. **G.** As in D, for circuits with both reciprocal and divergent feedback inhibition. **H.** As in D, for circuits containing only divergent inhibition. **I.** Effect of cell type-specific inactivation on MGB rate for heterogeneous inhibitory feedback connections between TRN and thalamic cells. Divergence ratio is the percent of trials that included divergent synapses. Reciprocal ratio is the percent of trials that included reciprocal TRN-MGB synapses. Middle, with electrical coupling between PV and SST cells. Bottom, effect of inactivation on MGB rate with heterogeneous inhibitory connections in addition to lateral inhibition from the SST^{TRN} to PV^{TRN} cells.

632 ## DISCUSSION

633 Differences between intrinsic physiology, synaptic connections, and axonal projections of distinct
634 cell types have been described for the GABAergic neurons of the TRN [42–45], but the impact of those
635 differences on their inhibitory modulation of thalamic processing remains unknown. We used a combination
636 of viral anatomical tracing, optogenetics, and awake *in-vivo* electrophysiological recordings along with
637 computational modeling to study the functional roles of audTRN PV and SST neurons in modulating sound
638 responses in the MGB[46]. Our results confirm that PV and SST neurons project to hierarchically distinct
639 sensory thalamic regions: while PV^{TRN} neurons primarily project to the center of the primary or first-order
640 auditory thalamic sub-region vMGB, SST^{TRN} neurons project almost exclusively to the dorsal subregions of
641 MGB and higher-order auditory thalamus (**Figure 1**). Here, we performed recordings in awake mice to
642 examine the effects of PV and SST neuron activation on the intact auditory circuit. We found that
643 inactivating these distinct subpopulations of audTRN inhibitory neurons had diverging effects on auditory
644 tone responses of MGB neurons **(Figure 2)**. While inactivation of PV^{TRN} neurons facilitated a large fraction
645 of MGB neurons, we also found that inactivation of some PV^{TRN} and all SST^{TRN} neurons suppressed a large
646 fraction of responses (**Figures 2, 3, 4**). Our results show that inactivation of both PV^{TRN} and SST^{TRN} neurons
647 change the frequency tuning of MGB neurons **(Figure 5)**. In addition, computational models allowed us to
648 identify several embedded variations of circuitry between TRN and MGB that could enable the experimental
649 observations (**Figure 6**).

650 Together, our anatomical, electrophysiological, and simulation results indicate complex roles for
651 TRN inhibition on MGB neurons and suggest a larger degree of divergence than what has been suggested
652 from the anatomical work here and by others[42,43]. A variety of connection schemes have been proposed for
653 TRN, including intra-TRN inhibition[59,59], lack of intra-TRN inhibition[58], typed reciprocal inhibition[42,43], and
654 open-loop or divergent connectivity to thalamic nuclei[63,64]. Cross-modal TRN responses have been
655 reported[65,66], offering further evidence of nuanced connectivity. In addition, gap junctions of the TRN could
656 be exclusive within one set or both sets of cell types or modality, or promiscuous across types[45], or absent in
657 adult tissue. Our computational survey of these possibilities suggests that divergence of TRN-MGB
658 connectivity is necessary, in addition to reciprocal inhibition, to achieve the bidirectional responses in MGB
659 observed for PV inactivation; and that some intra-TRN connectivity, whether gap junctional and/or
660 GABAergic, plays a role in allowing for the suppressive effects of SST inactivation. Our modeling offers

661 several predictions for future experiments, using optogenetic approaches. First, our model predicts a cell-
662 specific inhibitory connection from SST^{TRN} to PV^{TRN}. Second, divergent inhibition (*e.g.* from SST^{TRN} to vMGB
663 neurons) could also be evaluated in the same experiment. Moreover, our modeling predicts that SST^{TRN} in
664 that case are driven by higher order cells; thus inactivating the higher order population while also
665 inactivating the SST^{TRN} would potentially reverse the observed impact on vMGB responses during SST
666 silencing. Similar experiments in future studies could be applied to test a PV^{TRN}-d/mMGB connection.

667 One proposed mechanism for our results is the possibility of intra-TRN synapses between PV and
668 SST neurons, similar to the interactions in cortical regions[1]. Evidence for GABAergic synapses between
669 nearby TRN neurons in slice preparations is exceedingly sparse[58,67], but longer-range intra-TRN interactions
670 are possible, and reports of dendro-dendritic synapses have been reported in the TRN of the cat[68]. We find
671 an example of such a connection in slice recordings (**Supplementary Figure S8**). It has also been reported
672 that excitatory collateral inputs from thalamic relay nuclei drive excitatory input onto TRN neurons and
673 therefore activate TRN neurons[69]. It is also possible that the suppression effects in tone-responsive units of
674 the MGB is a direct result of fast feedback arising from excitatory MGB collaterals, intra-TRN dendro-
675 dendritic synapses, or other regions of GABAergic inputs to the TRN like the basal forebrain, substantia
676 nigra or lateral hypothalamus[70–73].

677 The TRN receives diverse modulatory inputs, including projections from the substantia nigra
678 reticulata[72], the basal forebrain[73–75], globus pallidus[76–78] and hypothalamus[71]. Whether these inputs are cell
679 type-specific is unknown. Our results indicate that the impact of inhibiting or modulating specific TRN
680 neuron types is complex and raises interest in the types, sources, and targets of modulatory input to the
681 thalamocortical pathways, along with the function of these projections. For example, inhibition of TRN
682 neurons that results in specific suppression or facilitation of the thalamocortical relay could be a mechanism
683 for modulating sensory perception in line with behavioral state. Indeed, recent studies have shown the
684 contributions of MGB to associative behavior memory tasks[79]. Whether and how disruption of inhibitory cell
685 types of the TRN affects behavioral outputs of the MGB has yet to be explored. Our results suggest that PV^{TRN}
686 and SST^{TRN} neurons may play distinct roles in behaviors that rely on lemniscal versus non-lemniscal
687 thalamic function.

688 Our experiments and analyses do not account for the feedback provided to MGB and TRN from the
689 cortex. Within the auditory thalamus, the TRN provides the majority of inhibition to the MGB, however,

690 MGB neurons also receive feedback from corticothalamic neurons in L5/L6 of AC as well as input from other
691 association areas, such as the BLA[33,80,81]. It is possible that the suppressive effects we observed included a
692 component of fast feedback inhibition from another region of the brain, or polysynaptic interactions. Future
693 studies using high-density channel probes to record from multiple brain areas simultaneously could further
694 our understanding of inhibitory circuit mechanisms. For example, recording from the TRN-MGB-AC circuit
695 simultaneously while optogenetically manipulating 1) corticothalamic feedback, 2) TRN-MGB inhibitory
696 synapses, or 3) collateral inputs from MGB to the TRN would allow recording effects of audTRN on neural
697 responses along the auditory pathway. An extensive anatomical tracing study would also specifically identify
698 possible sources of GABAergic input to PV and SST neurons involved in the auditory pathway. This could
699 reveal possible sources of feedback inhibitory inputs to the TRN that might drive the tone-evoked
700 suppression we observe in our study.

701 Combined, our results provide an insight into the complexity of the audTRN and identify cell-type
702 specific mechanisms for controlling sound processing in the auditory thalamus.

703

704 ## RESOURCE AVAILABILITY

705 ### Lead Contact

706 Further information and requests for resources and reagents should be directed to and will be
707 fulfilled by the Lead Contact, Maria Geffen (mgeffen@pennmedicine.upenn.edu).

708

709 ### Data & Code availability

710 Source data has been deposited in Dryad: https://doi.org/10.5061/dryad.ht76hdrq5. Data analysis
711 code is available on GitHub: https://github.com/geffenlab/Rolon_Martinez_2024. Code for the model is
712 available at github: https://github.com/jhaaslab/TRN_MGB_celltypespecific.

713

714 ### Acknowledgements

715 The authors would like to thank the members of the Geffen and Haas laboratories and Yale Cohen for their
716 discussions and helpful comments. This work was supported by the following grants from NIDCD:
717 R01DC15527, R01DC014479, R03DC013660 to MNG, F31DC018473 to SRM, F31DC016524to CFA, from
718 NINDS R01NS113241 to MNG and NIH R01 NS128713 to JSH.

719

720 ## REFERENCES

721 1. Blackwell, J.M., and Geffen, M.N. (2017). Progress and challenges for understanding the function of
722 cortical microcircuits in auditory processing. Nat. Commun. *8*, 2165. https://doi.org/10.1038/s41467-
723 017-01755-2.

724 2. Chen, Q.C., and Jen, P.H. (2000). Bicuculline application affects discharge patterns, rate-intensity
725 functions, and frequency tuning characteristics of bat auditory cortical neurons. Hear. Res. *150*, 161–
726 174. https://doi.org/10.1016/s0378-5955(00)00197-0.

727 3. Wu, G.K., Arbuckle, R., Liu, B.H., Tao, H.W., and Zhang, L.I. (2008). Lateral sharpening of cortical
728 frequency tuning by approximately balanced inhibition. Neuron *58*, 132–143.
729 https://doi.org/10.1016/j.neuron.2008.01.035.

730 4. Wang, J., Caspary, D., and Salvi, R.J. (2000). GABA-A antagonist causes dramatic expansion of tuning in
731 primary auditory cortex. Neuroreport *11*, 1137–1140.

732 5. Pollak, G.D., Xie, R., Gittelman, J.X., Andoni, S., and Li, N. (2011). The dominance of inhibition in the
733 inferior colliculus. Hear. Res. *274*, 27–39. https://doi.org/10.1016/j.heares.2010.05.010.

734 6. Myoga, M.H., Lehnert, S., Leibold, C., Felmy, F., and Grothe, B. (2014). Glycinergic inhibition tunes
735 coincidence detection in the auditory brainstem. Nat. Commun. *5*, 3790.
736 https://doi.org/10.1038/ncomms4790.

737 7. Burger, R.M., Fukui, I., Ohmori, H., and Rubel, E.W. (2011). Inhibition in the balance: binaurally
738 coupled inhibitory feedback in sound localization circuitry. J. Neurophysiol. *106*, 4–14.
739 https://doi.org/10.1152/jn.00205.2011.

740 8. Natan, R.G., Briguglio, J.J., Mwilambwe-Tshilobo, L., Jones, S.I., Aizenberg, M., Goldberg, E.M., and
741 Geffen, M.N. (2015). Complementary control of sensory adaptation by two types of cortical
742 interneurons. eLife *4*. https://doi.org/10.7554/eLife.09868.

743 9. Natan, R.G., Rao, W., and Geffen, M.N. (2017). Cortical Interneurons Differentially Shape Frequency
744 Tuning following Adaptation. Cell Rep. *21*, 878–890. https://doi.org/10.1016/j.celrep.2017.10.012.

745 10. Aizenberg, M., Mwilambwe-Tshilobo, L., Briguglio, J.J., Natan, R.G., and Geffen, M.N. (2015).
746 Bidirectional Regulation of Innate and Learned Behaviors That Rely on Frequency Discrimination by
747 Cortical Inhibitory Neurons. PLoS Biol. *13*, 1–32. https://doi.org/10.1371/journal.pbio.1002308.

748 11. Briguglio, J.J., Aizenberg, M., Balasubramanian, V., and Geffen, M.N. (2018). Cortical neural activity
749 predicts sensory acuity under optogenetic manipulation. J. Neurosci. *38*, 2094–2105.
750 https://doi.org/10.1523/JNEUROSCI.2457-17.2017.

751 12. Park, Y., and Geffen, M.N. (2019). A Unifying Mechanistic Model of the Auditory Cortex with Inhibitory
752 Subtypes. bioRxiv, 626358. https://doi.org/10.1101/626358.

753 13. Phillips, E.A., and Hasenstaub, A.R. (2016). Asymmetric effects of activating and inactivating cortical
754 interneurons. eLife *5*. https://doi.org/10.7554/eLife.18383.

755 14. Phillips, E.A.K., Schreiner, C.E., and Hasenstaub, A.R. (2017). Cortical Interneurons Differentially
756 Regulate the Effects of Acoustic Context. Cell Rep. *20*, 771–778.
757 https://doi.org/10.1016/j.celrep.2017.07.001.

15. Moore, A.K., and Wehr, M. (2013). Parvalbumin-expressing inhibitory interneurons in auditory cortex are well-tuned for frequency. J. Neurosci. *33*, 13713–13723. https://doi.org/10.1523/JNEUROSCI.0663-13.2013.

16. Li, L.Y., Xiong, X.R., Ibrahim, L.A., Yuan, W., Tao, H.W., and Zhang, L.I. (2015). Differential Receptive Field Properties of Parvalbumin and Somatostatin Inhibitory Neurons in Mouse Auditory Cortex. Cereb. Cortex *25*, 1782–1791. https://doi.org/10.1093/cercor/bht417.

17. Hamilton, L.S., Sohl-Dickstein, J., Huth, A.G., Carels, V.M., Deisseroth, K., and Bao, S. (2013). Optogenetic Activation of an Inhibitory Network Enhances Feedforward Functional Connectivity in Auditory Cortex. Neuron *80*, 1066–1076. https://doi.org/10.1016/j.neuron.2013.08.017.

18. Seybold, B.A., Phillips, E.A.K., Schreiner, C.E., and Hasenstaub, A.R. (2015). Inhibitory Actions Unified by Network Integration. Neuron *87*, 1181–1192. https://doi.org/10.1016/J.NEURON.2015.09.013.

19. Ulanovsky, N., Las, L., and Nelken, I. (2003). Processing of low-probability sounds by cortical neurons. Nat. Neurosci. *6*, 391–398. https://doi.org/10.1038/nn1032.

20. Taaseh, N., Yaron, A., and Nelken, I. (2011). Stimulus-Specific Adaptation and Deviance Detection in the Rat Auditory Cortex. PLoS ONE *6*, e23369. https://doi.org/10.1371/journal.pone.0023369.

21. Fishman, Y.I., and Steinschneider, M. (2012). Searching for the mismatch negativity in primary auditory cortex of the awake monkey: Deviance detection or stimulus specific adaptation? J. Neurosci. *32*, 15747–15758. https://doi.org/10.1523/JNEUROSCI.2835-12.2012.

22. Farley, B.J., Quirk, M.C., Doherty, J.J., and Christian, E.P. (2010). Stimulus-Specific Adaptation in Auditory Cortex Is an NMDA-Independent Process Distinct from the Sensory Novelty Encoded by the Mismatch Negativity. J. Neurosci. *30*, 16475–16484. https://doi.org/10.1523/JNEUROSCI.2793-10.2010.

23. Polterovich, A., Jankowski, M.M., and Nelken, I. (2018). Deviance sensitivity in the auditory cortex of freely moving rats. PLoS ONE *13*, e0197678. https://doi.org/10.1371/journal.pone.0197678.

24. Bartlett, E.L. (2013). The organization and physiology of the auditory thalamus and its role in processing acoustic features important for speech perception. Brain Lang. *126*, 29–48. https://doi.org/10.1016/j.bandl.2013.03.003.

25. He, J. (2003). Corticofugal modulation of the auditory thalamus. Exp. Brain Res. *153*, 579–590. https://doi.org/10.1007/s00221-003-1680-5.

26. Crabtree, J.W. (1998). Organization in the auditory sector of the cat's thalamic reticular nucleus. J. Comp. Neurol. *390*, 167–182. https://doi.org/10.1002/(sici)1096-9861(19980112)390:2<167::aid-cne1>3.0.co;2-%23.

27. Crabtree, J.W. (2018). Functional diversity of thalamic reticular subnetworks. Front. Syst. Neurosci. *12*, 41. https://doi.org/10.3389/FNSYS.2018.00041/BIBTEX.

28. Houser, C.R., Vaughn, J.E., Barber, R.P., and Roberts, E. (1980). GABA neurons are the major cell type of the nucleus reticularis thalami. Brain Res. *200*, 341–354. https://doi.org/10.1016/0006-8993(80)90925-7.

29. Pinault, D. (2004). The thalamic reticular nucleus: structure, function and concept. Brain Res. Rev. *46*, 1–31. https://doi.org/10.1016/J.BRAINRESREV.2004.04.008.

30. Guillery, R.W., and Sherman, S.M. (2002). Thalamic relay functions and their role in corticocortical communication: generalizations from the visual system. Neuron *33*, 163–175.

31. Carroll, B.J., Sampathkumar, V., Kasthuri, N., and Sherman, S.M. (2022). Layer 5 of cortex innervates the thalamic reticular nucleus in mice. Proc. Natl. Acad. Sci. U. S. A. *119*. https://doi.org/10.1073/PNAS.2205209119.

32. Gentet, L.J., and Ulrich, D. (2004). Electrophysiological characterization of synaptic connections between layer VI cortical cells and neurons of the nucleus reticularis thalami in juvenile rats. Eur. J. Neurosci. *19*, 625–633. https://doi.org/10.1111/j.1460-9568.2004.03168.x.

33. Guo, W., Clause, A.R., Barth-Maron, A., and Polley, D.B. (2017). A Corticothalamic Circuit for Dynamic Switching between Feature Detection and Discrimination. Neuron *95*, 180-194.e5. https://doi.org/10.1016/j.neuron.2017.05.019.

34. Lam, Y.W., and Sherman, S.M. (2005). Mapping by laser photostimulation of connections between the thalamic reticular and ventral posterior lateral nuclei in the rat. J. Neurophysiol. *94*, 2472–2483. https://doi.org/10.1152/jn.00206.2005.

35. Lam, Y.W., and Sherman, S.M. (2011). Functional organization of the thalamic input to the thalamic reticular nucleus. J. Neurosci. *31*, 6791–6799. https://doi.org/10.1523/JNEUROSCI.3073-10.2011.

36. Ahrens, S., Jaramillo, S., Yu, K., Ghosh, S., Hwang, G.R., Paik, R., Lai, C., He, M., Huang, Z.J., and Li, B. (2015). ErbB4 regulation of a thalamic reticular nucleus circuit for sensory selection. Nat. Neurosci. *18*, 104–111. https://doi.org/10.1038/nn.3897.

37. Crick, F. (2006). Function of the thalamic reticular complex: the searchlight hypothesis. Proc. Natl. Acad. Sci. *81*, 4586–4590. https://doi.org/10.1073/pnas.81.14.4586.

38. Halassa, M.M., Chen, Z., Wimmer, R.D., Brunetti, P.M., Zhao, S., Zikopoulos, B., Wang, F., Brown, E.N., and Wilson, M.A. (2014). State-dependent architecture of thalamic reticular subnetworks. Cell *158*, 808–821. https://doi.org/10.1016/j.cell.2014.06.025.

39. Nakajima, M., Schmitt, L.I., and Halassa, M.M. (2019). Prefrontal Cortex Regulates Sensory Filtering through a Basal Ganglia-to-Thalamus Pathway. Neuron *103*, 445-458.e10. https://doi.org/10.1016/j.neuron.2019.05.026.

40. Schmitt, L.I., Wimmer, R.D., Nakajima, M., Happ, M., Mofakham, S., and Halassa, M.M. (2017). Thalamic amplification of cortical connectivity sustains attentional control. Nature *545*, 219–223. https://doi.org/10.1038/nature22073.

41. Wimmer, R.D., Schmitt, L.I., Davidson, T.J., Nakajima, M., Deisseroth, K., and Halassa, M.M. (2015). Thalamic control of sensory selection in divided attention. Nature *526*, 705–709. https://doi.org/10.1038/nature15398.

42. Martinez-Garcia, R.I., Voelcker, B., Zaltsman, J.B., Patrick, S.L., Stevens, T.R., Connors, B.W., Cruikshank, S.J., and Carney, N.D. (2020). Two dynamically distinct circuits drive inhibition in the sensory thalamus. Nature *583*. https://doi.org/10.1038/s41586-020-2512-5.

43. Clemente-Perez, A., Makinson, S.R., Higashikubo, B., Brovarney, S., Cho, F.S., Urry, A., Holden, S.S., Wimer, M., Dávid, C., Fenno, L.E., et al. (2017). Distinct Thalamic Reticular Cell Types Differentially Modulate Normal and Pathological Cortical Rhythms. Cell Rep. *19*, 2130–2142. https://doi.org/10.1016/j.celrep.2017.05.044.

44. Li, Y., Lopez-Huerta, V.G., Adiconis, X., Levandowski, K., Choi, S., Simmons, S.K., Arias-Garcia, M.A., Guo, B., Yao, A.Y., Blosser, T.R., et al. (2020). Distinct subnetworks of the thalamic reticular nucleus. Nature *583*. https://doi.org/10.1038/s41586-020-2504-5.

45. Vaughn, M.J., Laswick, Z., Wang, H., and Haas, J.S. (2024). Functionally Distinct Circuits Are Linked by Heterocellular Electrical Synapses in the Thalamic Reticular Nucleus. eNeuro *11*. https://doi.org/10.1523/ENEURO.0269-23.2023.

46. Rolón Martínez, S. (2023). Role of Inhibitory Neuron Types of the TRN in Auditory Processing. Ph.D. Thesis. ProQuest Dissertations & Theses University of Pennsylvania. 30574161.

47. Johnson, K.R., Tian, C., Gagnon, L.H., Jiang, H., Ding, D., and Salvi, R. (2017). Effects of Cdh23 single nucleotide substitutions on age-related hearing loss in C57BL/6 and 129S1/Sv mice and comparisons with congenic strains. Sci. Rep. *7*, 44450. https://doi.org/10.1038/srep44450.

48. Siegle, J.H., López, A.C., Patel, Y.A., Abramov, K., Ohayon, S., and Voigts, J. (2017). Open Ephys: an open-source, plugin-based platform for multichannel electrophysiology. J. Neural Eng. *14*, 045003. https://doi.org/10.1088/1741-2552/aa5eea.

49. Pachitariu, M., Sridhar, S., and Stringer, C. (2023). Solving the spike sorting problem with Kilosort. Preprint at bioRxiv, https://doi.org/10.1101/2023.01.07.523036 https://doi.org/10.1101/2023.01.07.523036.

50. Stringer, C., Wang, T., Michaelos, M., and Pachitariu, M. (2021). Cellpose: a generalist algorithm for cellular segmentation. Nat. Methods *18*, 100–106. https://doi.org/10.1038/s41592-020-01018-x.

51. Destexhe, A., Bal, T., McCormick, D.A., and Sejnowski, T.J. (1996). Ionic mechanisms underlying synchronized oscillations and propagating waves in a model of ferret thalamic slices. J. Neurophysiol. *76*, 2049–2070. https://doi.org/10.1152/jn.1996.76.3.2049.

52. Pham, T., and Haas, J.S. (2018). Electrical synapses between inhibitory neurons shape the responses of principal neurons to transient inputs in the thalamus: a modeling study. Sci. Rep. *8*, 7763. https://doi.org/10.1038/s41598-018-25956-x.

53. Traub, R.D., Contreras, D., Cunningham, M.O., Murray, H., LeBeau, F.E.N., Roopun, A., Bibbig, A., Wilent, W.B., Higley, M.J., and Whittington, M.A. (2005). Single-Column Thalamocortical Network Model Exhibiting Gamma Oscillations, Sleep Spindles, and Epileptogenic Bursts. J. Neurophysiol. *93*, 2194–2232. https://doi.org/10.1152/jn.00983.2004.

54. Desai, N.V., and Varela, C. (2021). Distinct burst properties contribute to the functional diversity of thalamic nuclei. J. Comp. Neurol. *529*, 3726–3750. https://doi.org/10.1002/cne.25141.

55. Lu, E., Llano, D.A., and Sherman, S.M. (2009). Different distributions of calbindin and calretinin immunostaining across the medial and dorsal divisions of the mouse medial geniculate body. Hear. Res. *257*, 16–23. https://doi.org/10.1016/J.HEARES.2009.07.009.

871 56. Mahn, M., Gibor, L., Patil, P., Cohen-Kashi Malina, K., Oring, S., Printz, Y., Levy, R., Lampl, I., and Yizhar,
872 O. (2018). High-efficiency optogenetic silencing with soma-targeted anion-conducting
873 channelrhodopsins. Nat. Commun. *9*, 4125. https://doi.org/10.1038/s41467-018-06511-8.

874 57. Pham, T., and Haas, J.S. (2019). Electrical synapses regulate both subthreshold integration and
875 population activity of principal cells in response to transient inputs within canonical feedforward
876 circuits. PLOS Comput. Biol. *15*, e1006440. https://doi.org/10.1371/journal.pcbi.1006440.

877 58. Hou, G., Smith, A.G., and Zhang, Z.-W. (2016). Lack of intrinsic GABAergic connections in the thalamic
878 reticular nucleus of the mouse. J. Neurosci. *36*, 7246–7252.

879 59. Deleuze, C., and Huguenard, J.R. (2006). Distinct Electrical and Chemical Connectivity Maps in the
880 Thalamic Reticular Nucleus: Potential Roles in Synchronization and Sensation. J. Neurosci. *26*, 8633–
881 8645. https://doi.org/10.1523/JNEUROSCI.2333-06.2006.

882 60. Lam, Y.-W., Nelson, C.S., and Sherman, S.M. (2006). Mapping of the Functional Interconnections
883 Between Thalamic Reticular Neurons Using Photostimulation. J. Neurophysiol. *96*, 2593–2600.
884 https://doi.org/10.1152/jn.00555.2006.

885 61. Pinault, D., and Deschênes, M. (1998). Projection and innervation patterns of individual thalamic
886 reticular axons in the thalamus of the adult rat: A three-dimensional, graphic, and morphometric
887 analysis. J. Comp. Neurol. *391*, 180–203. https://doi.org/10.1002/(SICI)1096-
888 9861(19980209)391:2<180::AID-CNE3>3.0.CO;2-Z.

889 62. Shosaku, A., Kayama, Y., Sumitomo, I., Sugitani, M., and Iwama, K. (1989). Analysis of recurrent
890 inhibitory circuit in rat thalamus: Neurophysiology of the thalamic reticular nucleus. Prog. Neurobiol.
891 *32*, 77–102. https://doi.org/10.1016/0301-0082(89)90011-7.

892 63. Crabtree, J.W., Collingridge, G.L., and Isaac, J.T.R. (1998). A new intrathalamic pathway linking
893 modality-related nuclei in the dorsal thalamus. Nat. Neurosci. *1*, 389–394.
894 https://doi.org/10.1038/1603.

895 64. Crabtree, J.W., and Isaac, J.T.R. (2002). New Intrathalamic Pathways Allowing Modality-Related and
896 Cross-Modality Switching in the Dorsal Thalamus. J. Neurosci. *22*, 8754–8761.
897 https://doi.org/10.1523/JNEUROSCI.22-19-08754.2002.

898 65. Kimura, A. (2014). Diverse subthreshold cross-modal sensory interactions in the thalamic reticular
899 nucleus: implications for new pathways of cross-modal attentional gating function. Eur J Neurosci *39*,
900 1405–1418.

901 66. Kimura, A. (2024). Cross-modal sensitivities to auditory and visual stimulations in the first-order
902 somatosensory thalamic nucleus. Eur. J. Neurosci. *60*, 5621–5657. https://doi.org/10.1111/ejn.16510.

903 67. Landisman, C.E., and Coulon, P. (2024). A Mixed Electrical and Chemical Synapse in the Thalamic
904 Reticular Nucleus. J. Neurophysiol. https://doi.org/10.1152/jn.00339.2024.

905 68. Deschênes, M., Madariaga-Domich, A., and Steriade, M. (1985). Dendrodendritic synapses in the cat
906 reticularis thalami nucleus: a structural basis for thalamic spindle synchronization. Brain Res. *334*,
907 165–168. https://doi.org/10.1016/0006-8993(85)90580-3.

908 69. Yen, C.T., Conley, M., Hendry, S.H., and Jones, E.G. (1985). The morphology of physiologically
909 identified GABAergic neurons in the somatic sensory part of the thalamic reticular nucleus in the cat.
910 J. Neurosci. Off. J. Soc. Neurosci. *5*, 2254–2268. https://doi.org/10.1523/JNEUROSCI.05-08-
911 02254.1985.

912 70. Asanuma, C., and Porter, L.L. (1990). Light and electron microscopic evidence for a GABAergic
913 projection from the caudal basal forebrain to the thalamic reticular nucleus in rats. J. Comp. Neurol.
914 *302*, 159–172. https://doi.org/10.1002/cne.903020112.

915 71. Herrera, C.G., Cadavieco, M.C., Jego, S., Ponomarenko, A., Korotkova, T., and Adamantidis, A. (2015).
916 Hypothalamic feedforward inhibition of thalamocortical network controls arousal and consciousness.
917 Nat. Neurosci. *19*, 290–298. https://doi.org/10.1038/nn.4209.

918 72. Paré, D., Hazrati, L.N., Parent, A., and Steriade, M. (1990). Substantia nigra pars reticulata projects to
919 the reticular thalamic nucleus of the cat: a morphological and electrophysiological study. Brain Res.
920 *535*, 139–146. https://doi.org/10.1016/0006-8993(90)91832-2.

921 73. Asanuma, C. (1989). Axonal arborizations of a magnocellular basal nucleus input and their relation to
922 the neurons in the thalamic reticular nucleus of rats. Proc. Natl. Acad. Sci. *86*, 4746–4750.
923 https://doi.org/10.1073/pnas.86.12.4746.

924 74. Jourdain, A., Semba, K., and Fibiger, H.C. (1989). Basal forebrain and mesopontine tegmental
925 projections to the reticular thalamic nucleus: an axonal collateralization and immunohistochemical
926 study in the rat. Brain Res *505*, 55–65. https://doi.org/10.1016/0006-8993(89)90115-7.

927 75. Bickford, M.E., Gunluk, A.E., Van Horn, S.C., and Sherman, S.M. (1994). GABAergic projection from the
928 basal forebrain to the visual sector of the thalamic reticular nucleus in the cat. J Comp Neurol *348*,
929 481–510. https://doi.org/10.1002/cne.903480402.

930 76. Gandia, J.A., De Las Heras, S., Garcia, M., and Gimenez-Amaya, J.M. (1993). Afferent projections to the
931 reticular thalamic nucleus from the globus pallidus and the substantia nigra in the rat. Brain Res Bull
932 *32*, 351–358. https://doi.org/10.1016/0361-9230(93)90199-l.

933 77. Halassa, M.M., and Acsady, L. (2016). Thalamic Inhibition: Diverse Sources, Diverse Scales. Trends
934 Neurosci *39*, 680–693. https://doi.org/10.1016/j.tins.2016.08.001.

935 78. Cornwall, J., Cooper, J.D., and Phillipson, O.T. (1990). Projections to the rostral reticular thalamic
936 nucleus in the rat. Exp Brain Res *80*, 157–171. https://doi.org/10.1007/bf00228857.

937 79. Belén Pardi, M., Vogenstahl, J., Dalmay, T., Spanò, T., Pu, D.L., Naumann, L.B., Kretschmer, F.,
938 Sprekeler, H., and Letzkus, J.J. (2020). A thalamocortical top-down circuit for associative memory.
939 Science *370*, 844–848.
940 https://doi.org/10.1126/SCIENCE.ABC2399/SUPPL_FILE/ABC2399_PARDI_SM.PDF.

941 80. Lee, C.C., and Sherman, S.M. (2010). Drivers and Modulators in the Central Auditory Pathways. Front.
942 Neurosci. *4*, 79. https://doi.org/10.3389/neuro.01.014.2010.

943 81. Winer, J.A. (2005). Decoding the auditory corticofugal systems. Hear. Res. *207*, 1–9.
944 https://doi.org/10.1016/j.heares.2005.06.007.

945